

1 **Particle number concentrations and size distributions in the stratosphere: Implications of**  
2 **nucleation mechanisms and particle microphysics**

3 Fangqun Yu<sup>1</sup>, Gan Luo<sup>1</sup>, Arshad Arjunan Nair<sup>1</sup>, Sebastian Eastham<sup>2,3</sup>, Christina J. Williamson<sup>4</sup>,  
4 <sup>5,a</sup>, Agnieszka Kupc<sup>5,6</sup>, and Charles A. Brock<sup>5</sup>

5 <sup>1</sup> Atmospheric Sciences Research Center, University at Albany, Albany, New York, US

6 <sup>2</sup> Laboratory for Aviation and the Environment, Department of Aeronautics and Astronautics,  
7 Massachusetts Institute of Technology, Cambridge, MA 02139, USA

8 <sup>3</sup> Joint Program on the Science and Policy of Global Change, Massachusetts Institute of  
9 Technology, Cambridge, MA 02139, USA

10 <sup>4</sup> Cooperative Institute for Research in Environmental Sciences, University of Colorado,  
11 Boulder, CO 80309, USA

12 <sup>5</sup> Chemical Sciences Laboratory, National Oceanic and Atmospheric Administration, Boulder,  
13 CO 80305, USA

14 <sup>6</sup> Faculty of Physics, Aerosol Physics and Environmental Physics, University of Vienna, 1090  
15 Vienna, Austria

16 <sup>a</sup> now at: Climate Research Programme, Finnish Meteorological Institute, 00101 Helsinki,  
17 Finland and Institute for Atmospheric and Earth System Research/Physics, Faculty of Science,  
18 University of Helsinki, 00014 Helsinki, Finland.

19

20 Correspondence to: F. Yu ([fyu@albany.edu](mailto:fyu@albany.edu))

21

22 **Abstract.** While formation and growth of particles in the troposphere have been extensively  
23 studied in the past two decades, very limited efforts have been devoted to understanding these in  
24 the stratosphere. Here we use both Cosmics Leaving Outdoor Droplets (CLOUD) laboratory  
25 measurements taken under very low temperatures (205–223K) and Atmospheric Tomography  
26 Mission (ATom) in-situ observations of particle number size distributions (PNSD) down to 3 nm  
27 to constrain nucleation mechanisms and to evaluate model simulated particle size distributions in  
28 the lowermost stratosphere (LMS). We show that the binary homogenous nucleation (BHN)  
29 scheme used in most of the existing stratospheric aerosol injection (a proposed method of solar  
30 radiation modification) modeling studies overpredict the nucleation rates by 3–4 orders of

31 magnitude (when compared to CLOUD data) and particle number concentrations in the  
32 background LMS by a factor  $\sim 2-4$  (when compared to ATom data). Based on a recently developed  
33 kinetic nucleation model, which gives rates of both ion-mediated nucleation (IMN) and BHN at  
34 low temperatures in good agreement with CLOUD measurements, both BHN and IMN occur in  
35 the stratosphere. However, IMN rates are generally more than one order of magnitude higher than  
36 BHN rates and thus dominate nucleation in the background stratosphere. In the Southern  
37 Hemisphere (SH) LMS with minimum influence of anthropogenic emissions, our analysis shows  
38 that ATom measured PNSDs generally have four apparent modes. The model captures reasonably  
39 well the two modes (Aitken mode and the first accumulation mode) with the highest number  
40 concentrations and the size-dependent standard deviations. However, the model misses an apparent  
41 second accumulation mode peaking around 300–400 nm, which is in the size range important for  
42 aerosol direct radiative forcing. The bi-modal structure of accumulation mode particles has also  
43 been observed in the stratosphere well above tropopause and in the volcano-perturbed stratosphere.  
44 We suggest that this bi-modal structure may be caused by the effect of charges on coagulation and  
45 growth, which is not yet considered in any existing models and may be important in the  
46 stratosphere due to high ionization rates and long lifetime of aerosols. Considering the importance  
47 of accurate PNSDs for projecting realistic radiation forcing response to stratospheric aerosol  
48 injection (SAI), it is essential to understand and incorporate such potentially important processes  
49 in SAI model simulations and carry out further research to find out what other processes that the  
50 present models might have missed.

51

52

53

## 54 1. Introduction

55 Solar radiation modification (also known as solar geoengineering) approaches are being  
56 developed in response to the climate crisis (IPCC, 2021). They would temporarily offset climate  
57 change by reducing incoming sunlight, augmenting (currently inadequate) mitigation efforts and  
58 buying time to reduce atmospheric levels of CO<sub>2</sub>, which is the root cause of the climate crisis. A  
59 recent report by the National Academies of Sciences, Engineering and Medicine (NASEM)  
60 emphasizes the urgent need to have a comprehensive understanding of the feasibility and potential  
61 risks/benefits of solar climate intervention approaches (NASEM, 2021). Stratospheric aerosol  
62 injection (SAI) has demonstrated the most promise as proximately engineerable (Shepherd et al.,  
63 2009; Lockley et al., 2020; IPCC, 2021) and has been extensively studied using models (e.g.,  
64 GeoMIP: Kravitz et al., 2011; GLENS: Mills et al., 2017; Richter et al., 2022). The NASEM report  
65 (NASEM, 2021) pointed out that “the overall magnitude and spatial distribution of the forcing  
66 produced by SAI depends strongly on the aerosol size distribution” and “One of the research  
67 priorities for SAI is thus to address critical gaps in knowledge about the evolution of the aerosol  
68 particle size distribution”. In the stratosphere, sulfate aerosols are formed by nucleation, followed  
69 by condensational growth and coagulation, and lost by evaporation in the upper stratosphere and  
70 downward sedimentation into the troposphere (Turco et al., 1982). New particle formation (NPF)  
71 (or nucleation) affects not only the number abundance but also the size distributions of  
72 stratospheric particles (e.g., Brock et al., 1995; Lee et al., 2003). There is increasing evidence  
73 (Weisenstein et al., 2022, Laakso et al., 2022) that a careful treatment of microphysical processes  
74 is necessary for projecting realistic radiative forcing response to SAI.

75 The process of NPF under tropospheric conditions has been extensively explored over the last  
76 two decades through laboratory and field measurements, theoretical studies, and numerical  
77 simulations (e.g., Yu and Turco, 2000; Vehkamäki et al., 2002; Kulmala et al., 2004; Kirkby et al.,  
78 2011; Dawson et al., 2012; Zhang et al., 2012; Kürten et al., 2016; Yu et al., 2018; Kerminen et  
79 al., 2018; Lee et al., 2019). Although some of the advances in our understanding of nucleation  
80 gained in the last two decades can be applied to stratospheric conditions, focused studies  
81 specifically examining the mechanisms of NPF under stratospheric conditions are quite limited.  
82 Indeed, the H<sub>2</sub>SO<sub>4</sub>–H<sub>2</sub>O binary homogenous nucleation (BHN) parameterization developed two  
83 decades ago by Vehkamäki et al. (2002) (named BHN\_V2002 thereafter) has been widely used in  
84 SAI modeling studies when nucleation process is explicitly considered (e.g., Tilmes et al., 2015;  
85 Jones et al., 2021; Weisenstein et al., 2022). Tilmes et al. (2015) described a Geoengineering  
86 Model Intercomparison Project (GeoMIP) experiment designed for climate and chemistry models,  
87 using the stratospheric aerosol distribution derived from the ECHAM5-HAM microphysical model  
88 (Stier et al., 2005) which calculated nucleation rates with the BHN\_V2002 scheme. Both models  
89 (UKESM1 and CESM2-WACCM6) employed for a recent GeoMIP G6sulfur study (Jones et al.,  
90 2021) used the BHN\_V2002 scheme. In another recent SAI study based on three interactive  
91 stratospheric aerosol microphysics models (Weisenstein et al., 2022), two models (MAECHAM5-  
92 HAM and SOCOL-AER) used BHN\_V2002 scheme while the other (CESM2-WACCM) used an  
93 empirical nucleation scheme to calculate nucleation rate as a function of sulfuric acid concentration  
94 only (i.e, no dependence on temperature and relative humidity). To our knowledge, the  
95 performance of this widely used BHN\_V2002 under stratospheric conditions has not been  
96 carefully examined, probably due to the lack of suitable in situ measurements of freshly nucleated  
97 particles in the stratosphere for constraining the scheme. In this regard, particle size distributions  
98 down to 3 nm measured in-situ during the NASA Atmospheric Tomography Mission (ATom) in

99 the lowermost stratosphere (LMS) of both SH and NH in four different seasons (Williamson et al.,  
100 2019, 2021; Kupc et al., 2020; Brock et al., 2021) provide much-needed data to constrain our  
101 understanding of the nucleation and particle microphysics in the stratosphere. In addition, well-  
102 controlled CLOUD experiments taken under low temperature (within the range of stratosphere)  
103 can also be used to assess the performance of nucleation schemes under stratospheric conditions.  
104 Another important issue related to stratospheric particles is the role of ionization in nucleation. It  
105 is well established that nucleation of  $\text{H}_2\text{SO}_4\text{-H}_2\text{O}$  on ions is favored over homogenous nucleation  
106 (Hamill et al., 1982; Yu and Turco, 2000; Lovejoy et al., 2004; Kirkby et al. 2011; Yu et al., 2018)  
107 but the role of ionization in NPF in the stratosphere has not been considered in any previous SAI  
108 studies (to our knowledge) in spite of the very high ionization rates in the stratosphere.

109 In this study, we use both CLOUD laboratory measurements taken under very low  
110 stratospheric temperatures and ATom PNSD measurements in LMS to constrain nucleation  
111 mechanisms and model simulated particle size distributions. For 3-D simulation of size-resolved  
112 stratospheric aerosols, we use the GEOS-Chem with the unified tropospheric-stratospheric  
113 chemistry-transport model with the size-resolved advanced particle microphysics (APM) package.  
114

## 115 **2. Model and data**

### 116 **2.1 GEOS-Chem/APM**

117 The GEOS-Chem model is a global 3-D model of atmospheric composition (e.g., Bey et al.,  
118 2001) and is continuously being improved (e.g., Luo et al., 2020; Holmes et al., 2019; Keller et al.,  
119 2014; Murray et al., 2012; Pye and Seinfeld, 2010; van Donkelaar et al., 2008; Evans and Jacob,  
120 2005; Martin et al., 2003). The GEOS-Chem tropospheric–stratospheric unified chemistry  
121 extension (UCX; Eastham et al., 2014), now the standard GEOS-Chem configuration, implements  
122 stratospheric chemistry, calculation of J-values for shorter wavelengths, and improved modeling  
123 of high-altitude aerosols. Extension of the chemistry mechanism to include reactions relevant to  
124 the stratosphere enables the capturing of stratospheric responses and troposphere–stratosphere  
125 coupling. UCX adds 28 species and 104 kinetic reactions, including 8 heterogeneous reactions,  
126 along with 34 photolytic decompositions. Atomic oxygen [both  $\text{O}(^3\text{P})$  and  $\text{O}(^1\text{D})$ ] is explicitly  
127 modeled; although also of short lifetime in the stratosphere, these species are important in correctly  
128 modeling stratospheric chemistry. Photochemistry is extended up to the stratopause to high-energy  
129 photons (177 nm) using the Fast-JX model, which includes cross-section data for many species  
130 relevant to the troposphere and stratosphere. Photolysis rates respond to changes in the  
131 stratospheric ozone layer. Additional heterogeneous reactions (Kirner et al., 2011, Rotman et al.,  
132 2001, Shi et al., 2001) are included to capture seasonal ozone depletion.  $\text{H}_2\text{O}$  is treated as a  
133 chemically-active advected tracer within the stratosphere. These permit chemical feedbacks  
134 between stratospheric ozone and aerosols and tropospheric photochemistry. The improved GEOS-  
135 Chem with coupled stratospheric–tropospheric responses has been evaluated with sonde and  
136 satellite measurements of  $\text{O}_3$ ,  $\text{HNO}_3$ ,  $\text{H}_2\text{O}$ ,  $\text{HCl}$ ,  $\text{ClO}$ ,  $\text{NO}_2$  and stratospheric intrusions (Eastham  
137 et al., 2014; Gronoff et al., 2021; Knowland et al., 2022). Yu and Luo (2009) incorporated a size-  
138 resolved (sectional) APM package into GEOS-Chem, henceforth referred to as GC-APM. The  
139 APM separates secondary particles from primary particles, uses 40 bins to represent secondary  
140 particles with high size resolution for the size range important for the growth of nucleated particles  
141 to accumulation mode sizes, and contains options to calculate nucleation rates based on different

142 nucleation schemes. In ~~GEOS-Chem/GC~~-APM, nucleation is calculated before condensation using  
143 a time-splitting technique. Therefore, no competition between nucleation and condensation for  
144 sulfuric acid vapor is considered. In most conditions, nucleation consumes only a very small  
145 fraction (<1%) of sulfuric acid vapor in the air and the time splitting does not affect the results.  
146 When nucleation rate is high, reduced time step for nucleation and growth is used to ensure that  
147 the fraction of sulfuric acid vapor consumed by nucleation each time step is small. The GC-APM  
148 uses a semi-implicit scheme to calculate sulfuric acid condensation together with sulfuric acid gas  
149 phase production to ensure that the change of sulfuric acid vapor concentration is smooth. APM is  
150 fully coupled with GEOS-Chem in both the troposphere and stratosphere, ~~and is employed for the~~  
151 ~~present study.~~

152 In the present study we have carried out GEOS-Chem-UCX/APM global simulations from  
153 01/2015 to 05/2018, with the first 17 months as spin-up and the remaining period covering ATom  
154 1-4 periods (06/2016–05/2018). The horizontal resolution is  $4^{\circ} \times 5^{\circ}$  and there are 72 vertical layers.  
155 Emissions from different sources, regions, and species are computed via the Harvard-NASA  
156 Emissions Component (HEMCO) on a user-defined grid (Keller et al., 2014). Historical global  
157 anthropogenic emissions are based on the Community Emissions Data System (CEDS) inventory  
158 (Hoesly et al., 2018). Regional anthropogenic emissions over the United States, Canada, Europe,  
159 and East Asia are replaced by regional emission inventories of the National Emissions Inventory  
160 (NEI, [https://www.epa.gov/air-emissions-inventories/2017-national-emissions-inventory-nei-](https://www.epa.gov/air-emissions-inventories/2017-national-emissions-inventory-nei-data)  
161 [data](https://www.epa.gov/air-emissions-inventories/2017-national-emissions-inventory-nei-data)), the Air Pollutant Emission Inventory (APEI, [https://www.canada.ca/en/environment-](https://www.canada.ca/en/environment-climate-change/services/pollutants/air-emissions-inventory-overview.html)  
162 [climate-change/services/pollutants/air-emissions-inventory-overview.html](https://www.canada.ca/en/environment-climate-change/services/pollutants/air-emissions-inventory-overview.html)), the Co-operative  
163 Programme for Monitoring and Evaluation of the Long-range Transmission of Air Pollutants in  
164 Europe (EMEP, <https://www.emep.int/index.html>), and the MIX Asian emission inventory (Li et  
165 al., 2017), respectively. Monthly mean aircraft emissions are generated based on the Aviation  
166 Emissions Inventory v2.0 (Stettler et al., 2011). The aircraft particle emissions include nucleation  
167 mode sulfate particles (Emission index =  $2 \times 10^{17}$  /kg-fuel, mean diameter = 9 nm, based on Kärcher  
168 et al., 2000), and black carbon and primary organic carbon (POC) particles. Global biomass  
169 burning is taken from Global Fire Emissions Database version 4 (van der Werf et al., 2017). The  
170 volcanic emissions of SO<sub>2</sub> are taken from AeroCom point-source data (Carn et al., 2015). Fixed  
171 global surface boundary conditions are applied for N<sub>2</sub>O, CFCs, HCFCs, halons, OCS and long-  
172 lived organic chlorine species (Eastham et al., 2014).

## 174 2.2 Airborne ATom measurements of PNSD

175 Measurements are essential in advancing our understanding of stratospheric aerosol properties  
176 and the fundamental processes governing these properties. NASA's Atmospheric Tomography  
177 Mission (ATom; Wofsy et al., 2021; Thompson et al., 2022) is a multi-agency effort that provides  
178 global in situ aircraft observations of the vertical structure of aerosols from near surface to ~12 km  
179 altitude. PNSDs are measured using the NOAA Aerosol Microphysical Properties (AMP) package  
180 (Brock et al., 2019) comprising nucleation-mode aerosol size spectrometer(s) (NMASS)  
181 (Williamson et al. 2018), ultra-high-sensitivity aerosol spectrometer(s) (UHSAS) (Kupc et al.  
182 2018), and a laser aerosol spectrometer (LAS) covering aerosol sizes from 3 nm to 4.5 μm. The  
183 aerosol number abundance can be obtained by integrating the PNSD measurements.

## 185 2.3 The CLOUD (Cosmics Leaving Outdoor Droplets) measurements

186 Laboratory measurements of nucleation rates as a function of key controlled parameters have  
187 been carried out in a 26.1 m<sup>3</sup> stainless steel cylinder chamber at the European Organization for  
188 Nuclear Research (CERN), in the framework of the CLOUD experiment (Cosmics Leaving  
189 Outdoor Droplets) (e.g., Kirkby et al., 2011; Kürten et al., 2016; Dunne et al., 2016). Some of  
190 these experiments were conducted at the temperature in the range of those in the stratosphere  
191 (Kirkby et al., 2011; Dunne et al., 2016) which are used in this study to evaluate nucleation  
192 schemes under stratospheric conditions.

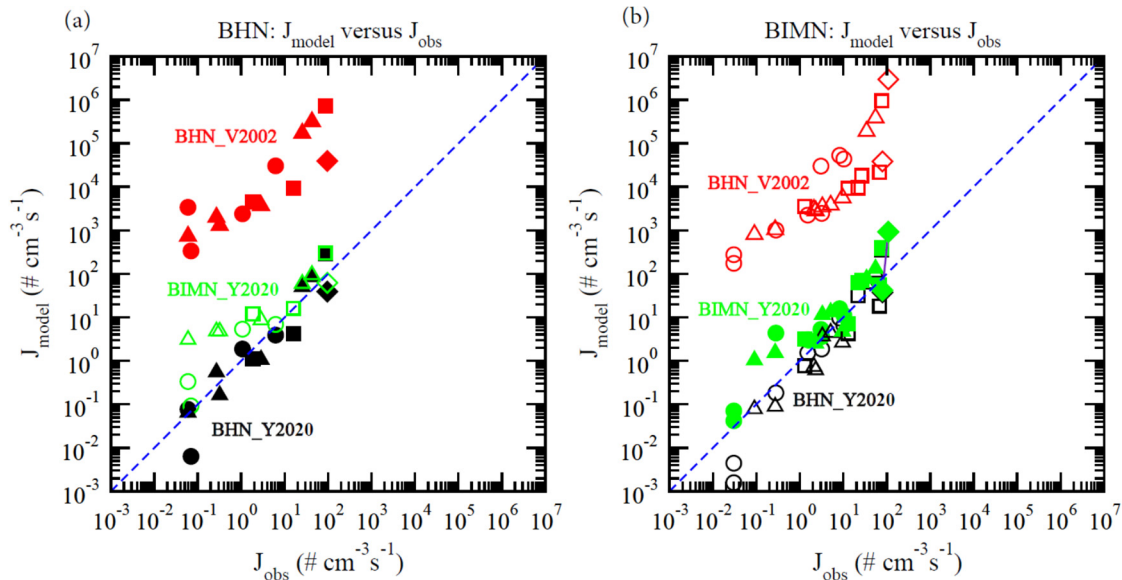
193

## 194 3. Results

### 195 3.1 H<sub>2</sub>SO<sub>4</sub>-H<sub>2</sub>O binary homogeneous nucleation (BHN) and binary ion-mediated nucleation 196 (BIMN) under stratospheric conditions

197 Nucleation is one of the microphysical processes influencing particle size distributions in the  
198 stratosphere (Turco et al., 1982) The CLOUD measurements under a wide range of well-controlled  
199 conditions (Kirkby et al., 2011; Dunne et al., 2016) provide a unique set of data to evaluate the  
200 nucleation theories. Yu et al. (2020) compared nucleation rates calculated based on a number of  
201 commonly used aerosol nucleation parameterizations with the CLOUD measurements. Here we  
202 specifically examine the comparison under stratospheric conditions where temperature is below ~  
203 230 K. Since ammonia concentrations in the stratosphere are generally negligible, we focus on  
204 binary nucleation in the present study. The contribution of organics to particle formation, growth,  
205 and compositions in the upper troposphere and LMS has been investigated in several studies (Kupc  
206 et al., 2020; Murphy et al., 2021; Williamson et al., 2021). Because of the lack of information with  
207 regard to the low volatile gaseous organic species, the possible role of organics in new particle  
208 formation in LWS is not considered in the present study.

209



210

211 **Figure 1.** Comparison of nucleation rates based on three different schemes with CLOUD  
212 measurements within the low temperature range ( $T = 205\text{--}223\text{ K}$ ) as that in the stratosphere for (a)  
213 binary homogeneous nucleation (no ionization) and (b) ion nucleation (at the presence of  
214 ionization rates  $2.51 - 110\text{ ion-pairs cm}^{-3}\text{s}^{-1}$ ). The different nucleation schemes shown are: BHN  
215 of Vehkamäki et al. (2002) (BHN\_V2002), BHN of Yu et al. (2020) (BHN\_Y2020), and BIMN

216 of Yu et al. (2020) (BIMN\_Y2020). For comparison, under binary condition of (a), BIMN rates at  
217  $Q = 20$  ion-pairs  $\text{cm}^{-3}\text{s}^{-1}$  are given while under binary ion nucleation condition of (b), BHN rates  
218 are also given. Values of  $\text{H}_2\text{SO}_4$  vapor concentration ( $[\text{H}_2\text{SO}_4]$ ) range from  $10^6$  to  $3 \times 10^7 \text{ cm}^{-3}$  and  
219 are separated into four groups in the plots (Circles:  $10^6 - 5 \times 10^6 \text{ cm}^{-3}$ ; triangles:  $5 \times 10^6 - 10^7 \text{ cm}^{-3}$ ;  
220 Squares:  $10^7 - 1.5 \times 10^7 \text{ cm}^{-3}$ ; Diamonds:  $1.5 \times 10^7 - 3 \times 10^7 \text{ cm}^{-3}$ ).

221  
222 Figure 1 compares nucleation rates based on the following three different schemes with  
223 CLOUD measurements under stratospheric temperature range ( $T = 205\text{--}223 \text{ K}$ ): BHN of  
224 Vehkamäki et al. (2002) (BHN\_V2002), BHN of Yu et al. (2020) (BHN\_Y2020), and BIMN of  
225 Yu et al. (2020) (BIMN\_Y2020). BHN\_V2002 and BHN\_Y2020 differ in term of thermodynamic  
226 data and nucleation approach used (Yu et al., 2020). To show the relative importance of  
227 homogeneous versus ion nucleation, BIMN rates at  $Q = 20$  ion-pairs  $\text{cm}^{-3}\text{s}^{-1}$  were given under  
228 binary homogeneous condition in Fig. 1a and BHN rates were also given under binary ion  
229 nucleation condition in Fig. 1b. Nucleation rates based on BHN\_V2002 are consistently 3–5 orders  
230 of magnitude higher than those observed under  $\text{H}_2\text{SO}_4\text{--H}_2\text{O}$  binary nucleation conditions without  
231 (Fig. 1a) and with (Fig. 1b) the effect of ionizations, while those based on BHN\_Y2020 and  
232 BIMN\_Y2020 are close to the observed values. It should be noted that similar to the CLOUD  
233 measurements with the effect of ionization, BHN rates are included in the BIMN rates (Yu et al.,  
234 2018) and the difference between BIMN and BHN rates indicates the contribution of ion mediated  
235 or induced nucleation. Under the conditions of Fig. 1a, assuming ionization rate of 20 ion-pairs  
236  $\text{cm}^{-3}\text{s}^{-1}$  (within the range of its typical value in the stratosphere) the BIMN rates are about one  
237 order of magnitude higher than BHN rates when the nucleation rates are below  $\sim 5 \text{ cm}^{-3}\text{s}^{-1}$  but  
238 close to BHN rates when nucleation rates are above  $\sim 5 \text{ cm}^{-3}\text{s}^{-1}$ . Similar difference between  
239 BHN\_Y2020 and BIMN\_Y2020 can also be seen in Fig. 1b, indicating the importance of ion  
240 nucleation at relatively lower nucleation rates (mostly associated with relatively lower  $[\text{H}_2\text{SO}_4]$ )  
241 and dominance of homogeneous nucleation at higher nucleation rates (associated with larger  
242  $[\text{H}_2\text{SO}_4]$ ). As we show next,  $[\text{H}_2\text{SO}_4]$  in the background stratosphere is generally quite low and  
243 thus ion nucleation dominates but BHN can become important in the  $\text{SO}_2$  plumes injected into the  
244 stratosphere.

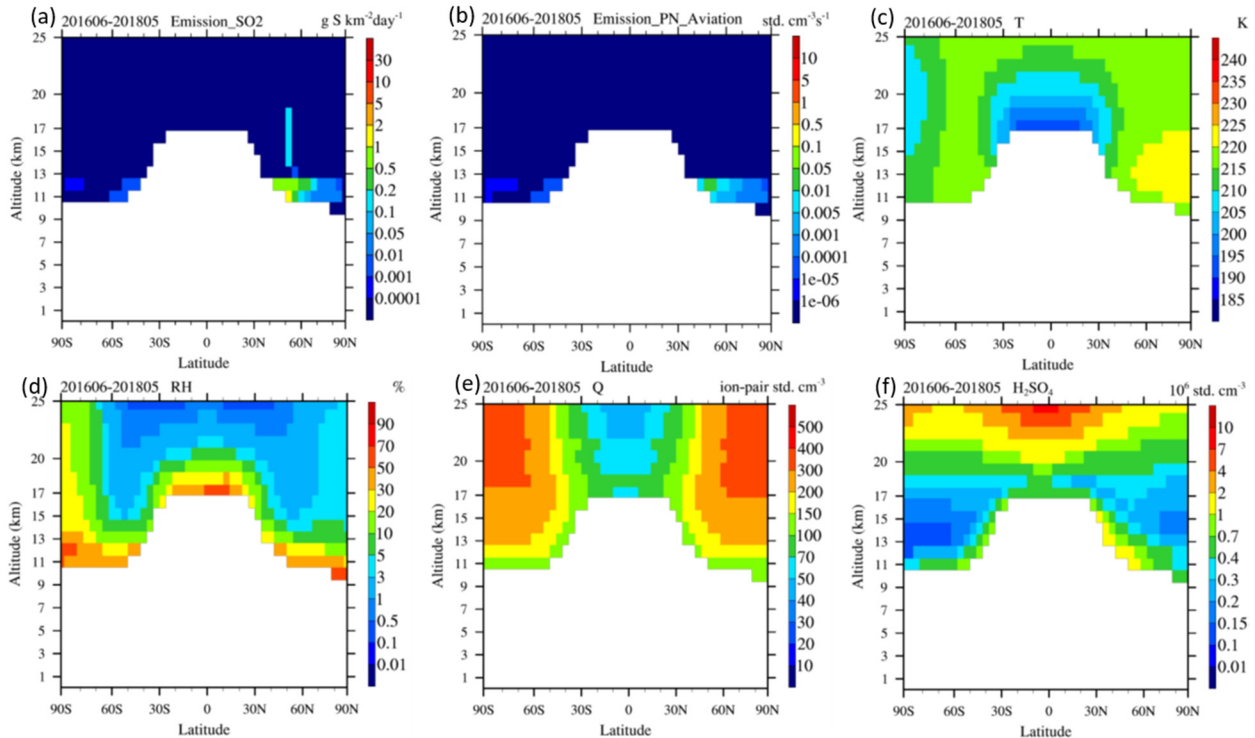
245

### 246 3.2 Nucleation rates and particle number concentrations in the stratosphere

247 Figure 2 shows the zonal mean  $\text{SO}_2$  emission ( $\text{SO}_2_{\text{emit}}$ ), particle number emitted by aviation  
248 ( $\text{PN}_{\text{aviation}}$ ), temperature ( $T$ ), relative humidity (RH), ionization rate ( $Q$ ), and  $[\text{H}_2\text{SO}_4]$  averaged  
249 during the two-year period (06/2016–05/2018) covering ATom 1-4. To focus on lower stratosphere  
250 (LS), only the values of these variables in the stratosphere (grid boxes with more than 50% time  
251 above tropopause) are shown. The  $\text{SO}_2$  emissions include all sources including volcanos and  
252 aviation. During this period, there was one relatively strong volcanic event, the Bezymianny  
253 volcano ( $55.98^\circ\text{N}$ ,  $160.59^\circ\text{E}$ ), on December 20, 2017 that injected  $5 \times 10^6 \text{ kg S}$  into an altitude of  $\sim$   
254  $14\text{--}18 \text{ km}$  (Carn et al., 2015). Aviation emission is generally limited to below  $\sim 12.5 \text{ km}$  altitude.  
255 Based on MERRA2 meteorology data, which is used to drive GEOS-Chem, almost all of grid  
256 boxes at  $12 \text{ km}$  are under the tropopause in the tropics ( $30^\circ\text{N}\text{--}30^\circ\text{S}$ ), most of grid boxes at  $12 \text{ km}$   
257 in the high latitude regions ( $60^\circ\text{N}\text{--}90^\circ\text{N}$ ,  $60^\circ\text{S}\text{--}90^\circ\text{S}$ ) are above tropopause, and some fractions of  
258 grid boxes at  $12 \text{ km}$  in the middle latitude regions ( $30^\circ\text{N}\text{--}60^\circ\text{N}$ ,  $30^\circ\text{S}\text{--}60^\circ\text{S}$ ) are above tropopause.  
259 As can be seen from Fig. 2b, some of aviation emissions in the middle and high latitude regions

260 are in the LMS, and the amount emitted into NH LMS is much higher (by several orders of  
 261 magnitude) than that in SH. The temperature in the LS ranges from 190–225K, with the lowest  
 262 value in the region just above tropical tropopause (Fig. 2c). RH in LS has highest values near  
 263 tropopause but drops quickly with increasing altitude, from ~30–50% near tropopause to ~0.1–1%  
 264 at ~ 25 km in the tropical and middle latitudes (Fig. 2d). The spatial variations of  $T$  and RH have  
 265 important effects on nucleation in LS. The cosmic ray induced ionization rate in LS has large  
 266 latitudinal gradient, ranging from ~40–100 ion-pair std.  $\text{cm}^{-3}\text{s}^{-1}$  (here “std.  $\text{cm}^{-3}$ ” refers to per cubic  
 267 centimeter at standard temperature and pressure, 273 K and 1013 hPa respectively) in the tropics  
 268 to 100–400 ion-pair std.  $\text{cm}^{-3}\text{s}^{-1}$  in middle and high latitude region (Fig. 2e). The high ionization  
 269 rates may have important implication for particle microphysics in LS, which will also be discussed  
 270 in Section 3.3.  $\text{H}_2\text{SO}_4$  is the most important aerosol precursor in LS and its concentration depends  
 271 on  $\text{SO}_2$  concentrations and oxidation, condensation sink, and its vapor pressure that depends on  $T$   
 272 and RH. The annual mean  $[\text{H}_2\text{SO}_4]$  (Fig. 2f) has large spatial variations, ranging from a minimum  
 273 of  $\sim 1\text{--}2 \times 10^5$  std.  $\text{cm}^{-3}$  at altitudes of  $\sim 12\text{--}15$  km in polar regions to  $\sim 4\text{--}20 \times 10^5$  std.  $\text{cm}^{-3}$  close  
 274 to the tropopause. From  $\sim 18\text{--}25$  km (well above the ATOm measurement altitude),  $[\text{H}_2\text{SO}_4]$   
 275 increases with altitude, mainly due to the increasing  $\text{H}_2\text{SO}_4$  vapor pressure associated with vertical  
 276 changes of  $T$  (Fig. 2c) and RH (Fig. 2d).

277  
 278



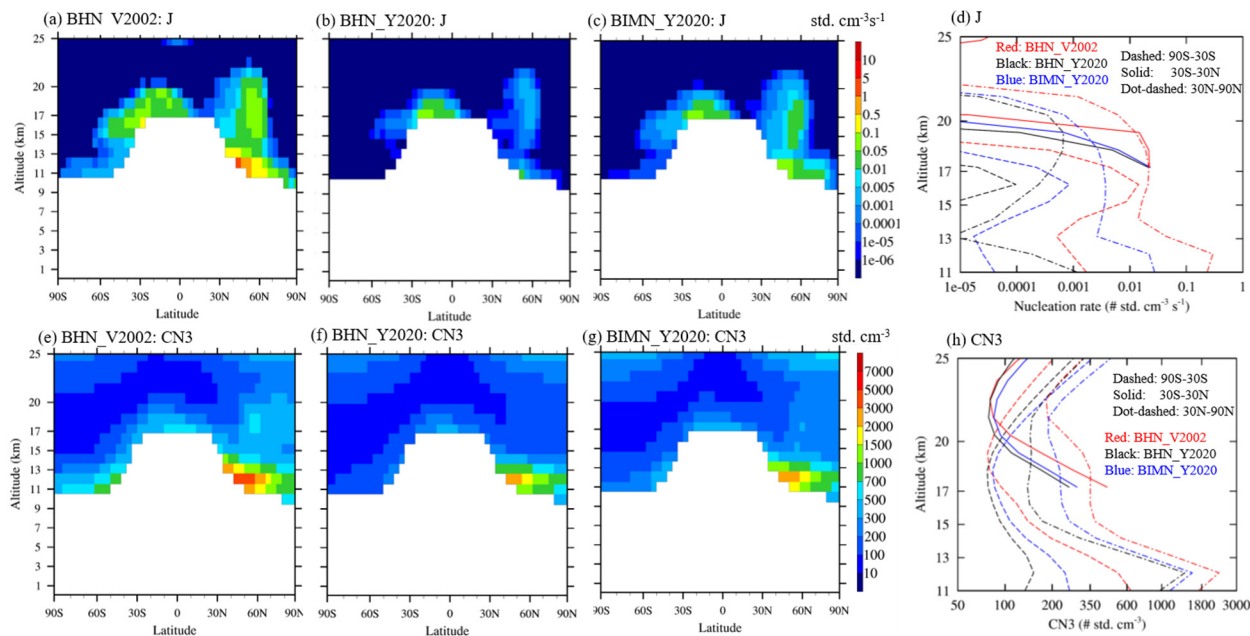
279 **Figure 2.** Zonal mean  $\text{SO}_2$ \_emit, PN\_Emit,  $T$ , RH,  $Q$ , and  $[\text{H}_2\text{SO}_4]$  averaged during the two-year  
 280 period (06/2016-05/2018) covering ATOm 1-4. To focus on the lower stratosphere, only the values  
 281 of these variables in grid boxes with more than 50% time above tropopause and below 25 km are  
 282 shown.  
 283

284



285 To demonstrate the effect of nucleation schemes on simulated aerosol properties, we compare  
286 in Fig. 3 zonal mean and vertical profiles of nucleation rates (J) and number concentrations of  
287 condensation nuclei larger than 3 nm (CN3) simulated based on the three nucleation schemes:  
288 BHN\_V2002, BHN\_Y2020, and BIMN\_Y2020. In all three schemes, the aviation emissions of  
289 both SO<sub>2</sub> (Fig. 2a) and particle numbers (Fig. 2b) are the same. The model simulations indicate  
290 that NPF occurs in the lower stratosphere but is mostly confined to LMS except in the area of  
291 volcano injection (for example, above ~ 14 km around ~ 52°N). There exist large differences in  
292 the nucleation rates predicted by the three schemes (noting the logarithmic color scale), with  
293 BHN\_V2002 rates generally 1–4 orders of magnitude higher while BIMN\_Y2020 rates ~ one  
294 order of magnitude higher than those based on BHN-Y2020. The difference between  
295 BIMN\_Y2020 and BHN\_V2002 rates are smaller in the LMS over tropics (30°S-30°N) where  
296 temperature is the lowest (see Fig. 2c). The magnitudes of differences are consistent with  
297 comparisons with CLOUD measurements (Fig. 1). The difference in nucleation rates leads to  
298 substantial difference in CN3 in LMS, with those based on BHN\_V2002 a factor 2–5 higher than  
299 those based on BHN\_Y2020 in LMS. LMS CN3 based on BIMN\_Y2020 is about 50% higher than  
300 that of BHN\_Y2020. Compared to the difference in nucleation rates, the differences in CN3 is  
301 much smaller. This is expected because on one hand only a small fraction of nucleated particles  
302 survive the coagulation scavenging and grow beyond 3 nm, and on the other hand direct emission  
303 of particle numbers from aviation (Fig. 2b; treated as direct emission but most of these are actually  
304 nucleated on chemi-ions in the exhaust plume shortly after emission) (Brock et al., 2000) and  
305 transport provide substantial amount of CN3 even without nucleation. Nevertheless, nucleation is  
306 still significant enough to affect the CN3. It is interesting to note that CN3 based on BIMN\_Y2020  
307 is higher at altitudes > ~ 22 km (Fig. 3h), which is associated with higher nucleation rates based  
308 on BIMN\_Y2020 than those based on BHN\_V2002 and BHN\_Y2020 within the altitude range of  
309 35-55 km. Another interesting point is that there is a much smaller vertical gradient in  
310 BHN\_V2002 nucleation rates in the tropical region (30S-30N) within ~ 17-20 km (see Figs. 3a  
311 and 3d), likely a result of different dependences of nucleation rates based on different schemes on  
312 T, RH, and [H<sub>2</sub>SO<sub>4</sub>] which have large vertical variations (see Fig. 2). It can be seen from Fig. 3  
313 that the simulations based on three nucleation schemes all show large hemispheric difference in  
314 particle number concentrations (by a factor of ~3-6) in LMS at middle and high latitudes,  
315 consistent with the ATom measurements (Williamson et al., 2021). Our sensitivity study (by  
316 turning off aviation emission, not shown, to be reported in a separate study) indicates this large  
317 hemispheric difference is largely caused by aviation emissions, confirming the analysis of  
318 Williamson et al. (2021).

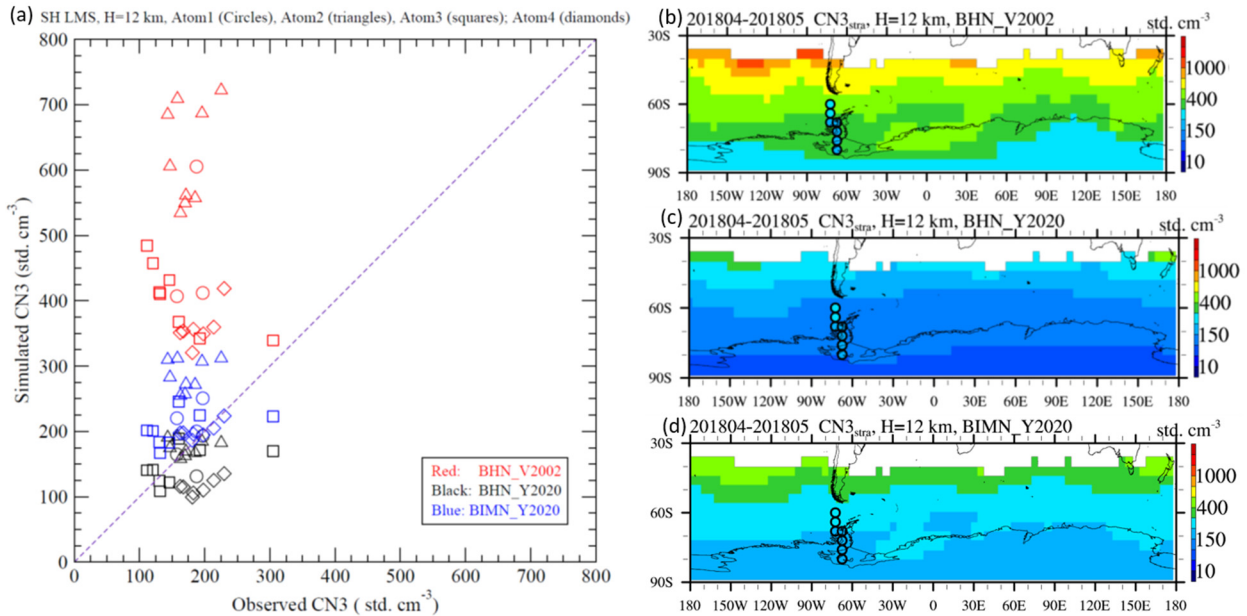
319



320  
 321 **Figure 3.** Model simulated zonal mean and vertical profiles of nucleation rates (J; upper panels)  
 322 and number concentrations of particles larger than 3 nm (CN3; lower panels) in the stratosphere  
 323 during the two-year period covering ATom 1-4 (06/2016- 05/2018), based on three nucleation  
 324 schemes (a&e: BHN\_V2002, b&f: BHN\_Y2020, and c&g: BIMN\_Y2020). The vertical profiles  
 325 in (d) and (h) are averaged for three latitude zones (90S-30S, 30S-30N, and 30N-90N). The values  
 326 for those grids with at least 50% of time above the tropopause are shown.

327  
 328 While it is difficult to observe nucleation rates in the stratosphere, the measurement of freshly  
 329 nucleated nanoparticles can be used to constrain nucleation schemes. Figure 4a compares the  
 330 model simulated CN3 (all particles with diameter larger than 3 nm, with the upper size limit of 12  
 331  $\mu\text{m}$  corresponding to the size of last model bin) based on the three nucleation schemes at altitudes  
 332 of around 12 km in SH middle and high altitudes during four seasons with the corresponding ATom  
 333 1–4 observations. As an example, Figures 4b–d show the model simulated horizontal distributions  
 334 of CN3 at 12 km altitude during ATom 4 with the values and locations of ATom4 CN3 data  
 335 overlaid. We choose SH for comparison, as it represents the background stratosphere with  
 336 minimum influence of anthropogenic emissions (i.e., aviation) (Fig. 2b), to avoid the uncertainty  
 337 associated with aviation emissions. In Figure 4, the model results are two-month average  
 338 corresponding to the flight months of each ATom campaign while the measurement data points  
 339 shown are those sampled within the altitudes range of 11.5–12.5 km, in the stratosphere  
 340 (ozone > 250 ppbv and RH < 10%, following the same stratosphere definitions as in Murphy et al.  
 341 (2021) and Williamson et al. (2021)), and averaged to a  $4^\circ \times 5^\circ$  gridbox for comparison with  
 342 modeled results. The impact of nucleation scheme on CN3 can be clearly seen: BHN\_V2002  
 343 overpredicted CN3 by a factor of 2–4, BHN\_Y2020 slightly underpredicted CN3, and  
 344 BIMN\_Y2020 slightly overpredicted CN3. The larger vertical spread in CN3 from BHN\_V2002  
 345 is caused by the large CN3 latitude gradient associated with higher nucleation near tropopause

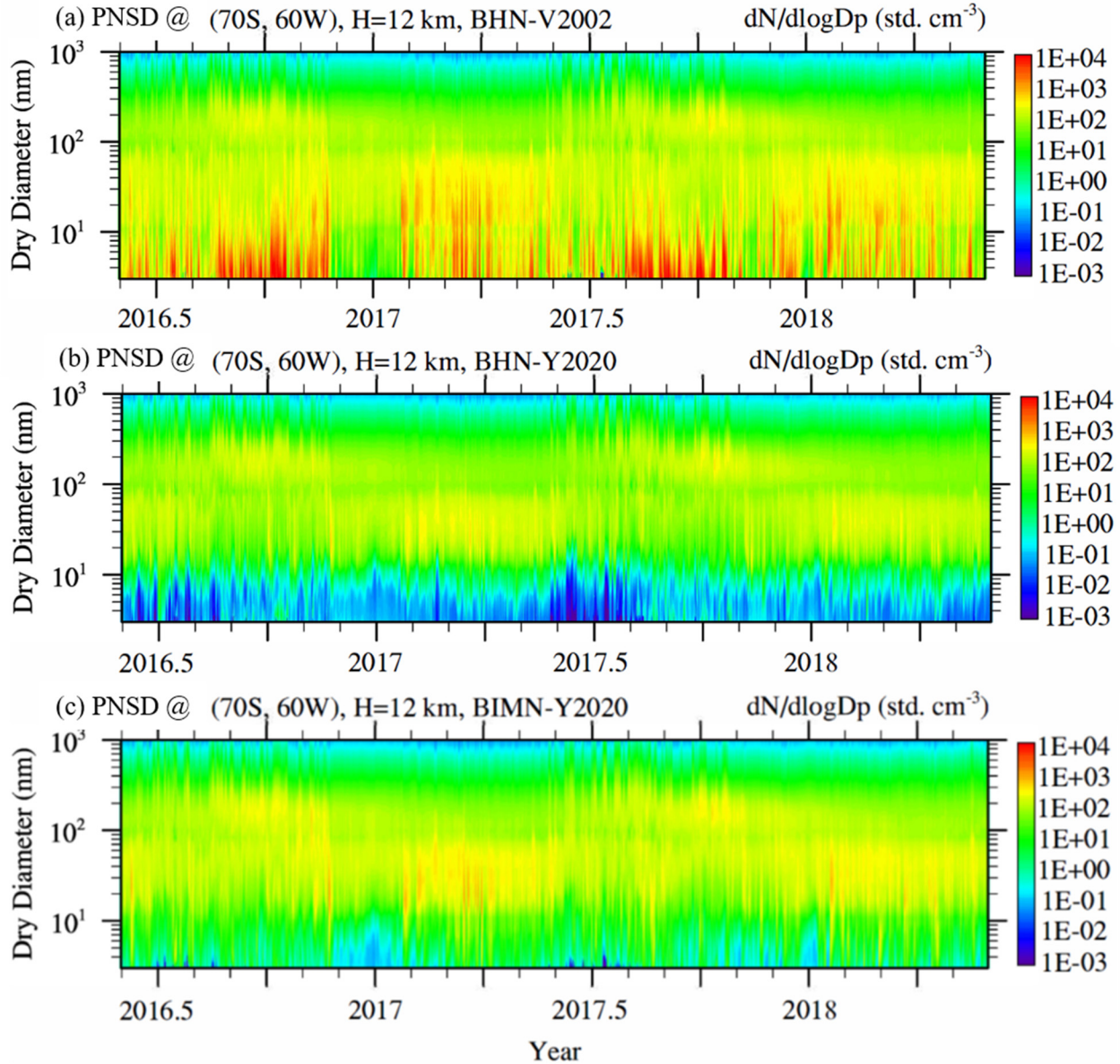
346 (Fig. 3). The comparisons above show that the ATom measurements provide a good constraint on  
 347 our understanding of the processes controlling CN3 in the LMS at mid-high latitudes.  
 348



349  
 350 **Figure 4.** CN3 at altitudes of around 12 km in SH middle and high latitudes: (a) Model simulated  
 351 versus observed during ATom 1-4 (Circles: ATom1; Triangles: ATom2; Sqaures: ATom3;  
 352 Diamonds: ATom4); (b-d) model simulated horizontal distributions corresponding to ATom 4  
 353 based on three different nucleation schemes (BHN\_V2002, BHN\_Y2020, and BIMN\_Y2020),  
 354 with the values and locations of ATom 4 CN3 measurements shown in the circles.

355  
 356 **3.3 PNSDs in the stratosphere**

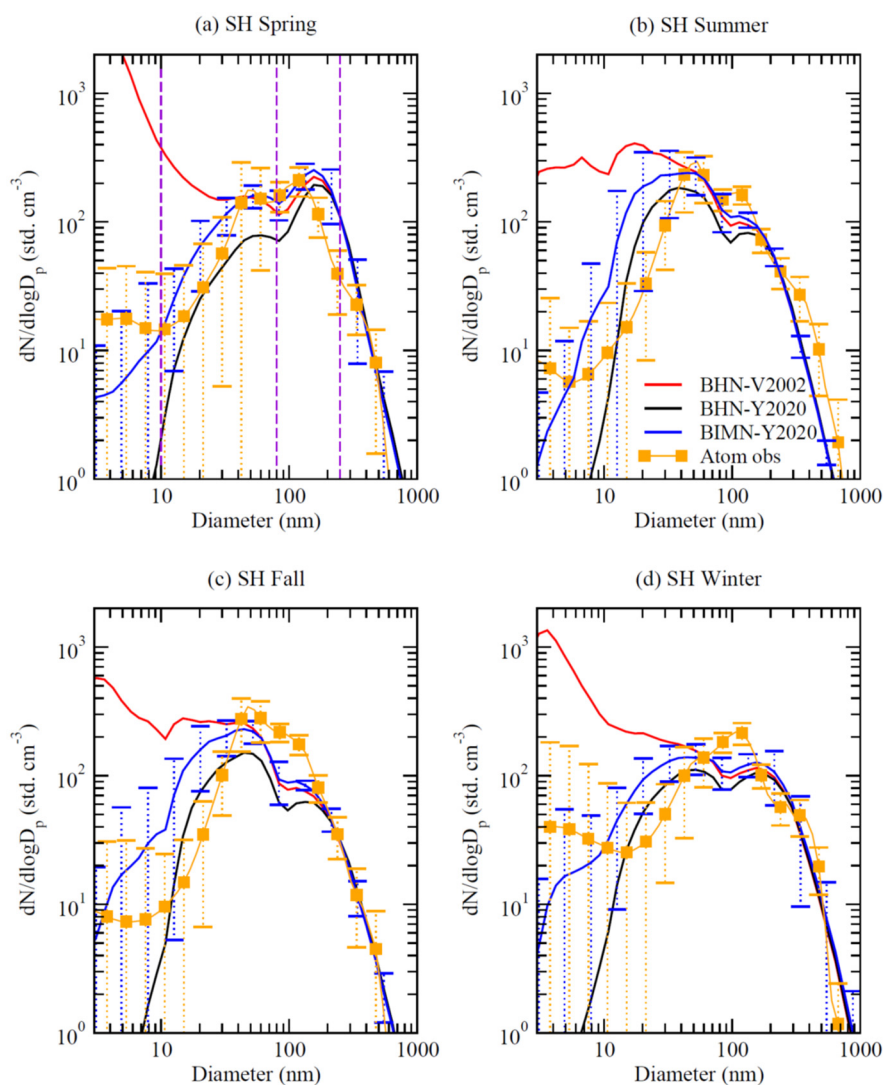
357 Figure 5 shows the model simulated evolution of PNSDs at an altitude of 12 km over a site in  
 358 SH (70°S, 60°W) during the two-year ATom period based on the three different nucleation  
 359 schemes. The PNSDs shown in Fig. 5 are averaged into four different seasons corresponding to  
 360 the months of ATom 1-4 field campaigns and are presented in Fig. 6 for comparison with the  
 361 observed mean PNSDs in SH LMS (Williamsons et al., 2021). It should be noted that modeled  
 362 PNSDs in Fig. 6 are two-month average at one fixed site at an altitude of 12 km (in the region  
 363 where many of SH LMS measurements were taken, see Fig. 4) while the observed ones are  
 364 averaged over all SH LMS air mass sampled during the corresponding ATom campaign. While  
 365 the comparison in Fig. 6 is not exactly coterminous, it allows us to make quantitative comparisons  
 366 of modeled and observed PNSDs. To take into account the variations in both model and observed  
 367 PNSDs, standard deviations are shown as error bars in the measured and modeled curves based on  
 368 BIMN\_Y2020.  
 369



370  
 371 **Figure 5.** Model simulated evolution of PNSDs at a site in SH (70S, 60 W) at altitude of 12 km  
 372 based on three nucleation schemes (BHN\_2002, BHN\_Y2020, and BIMN\_Y2020).

373  
 374 Figure 6 shows that PNSDs measured in the background LMS have multiple modes: a  
 375 nucleation mode (NuclM:  $\lesssim 10$  nm), an Aitken mode (AitkenM:  $\sim 10 - 80$  nm), and two  
 376 accumulation modes (AccuM1:  $\sim 80 - 250$  nm and AccuM2:  $\sim 250 - 700$  nm). It should be noted  
 377 that these modes are not the same size limits as those presented in the public ATom dataset. As  
 378 shown in Figures 5 and 6, the model based on all three nucleation schemes generally captures the  
 379 AitkenM and AccuM1 and the existence of a minimum in PNSDs around 80 nm, although there  
 380 exist differences. Interestingly, the relative height (or peak values of  $dN/d\log D_p$ ) of AitkenM and  
 381 AccuM1 has strong seasonal variations. The model captures a relatively higher AitkenM in SH  
 382 Summer and Fall and a higher AccuM1 in SH Spring. The model simulated PNSDs also agree

383 well with the measurements in term of the size-dependent normalized standard deviation ( $\sigma_N$ , i.e.,  
 384 the standard deviation  $\sigma$  divided by the mean): relatively smaller  $\sigma_N$  for AccuM1 and larger size  
 385 part of AitkenM and much larger  $\sigma_N$  for NuclM, smaller size part of AitkenM, and AccuM2. While  
 386 the larger  $\sigma_N$  for NuclM is understandable because of NPF, it is surprising for AccuM2. The  
 387 AccuM2 particles have relatively long lifetime and are expected to be well-mixed (and thus have  
 388 small variations) in LS. The transport of AccuM2 particles from UT may contribute to the larger  
 389 variations. Murphy et al. (2021) showed the chemical signature of this transported mode, and here  
 390 we show that the variation in the size distribution may also contain information about the mixing  
 391 of UT particles into LMS. Compared to the observations, the model simulated AccuM2  $\sigma_N$  are  
 392 larger in SH Winter and Spring but are smaller in SH Summer and Fall. The possible reasons for  
 393 the large variations of AccuM2 in LMS and the differences between model simulations and  
 394 measurements remain to be studied.



395  
 396 **Figure 6.** Model simulated seasonal mean PNSDs at a site in SH (70°S, 60°W) at altitude of 12  
 397 km based on three nucleation schemes and comparisons with the corresponding ATom  
 398 measurements (a: SH Spring 09–10/2017, b: SH Summer 01–02/2017, c: SH Fall 04–05/2018, and

399 d: SH Winter 06–07/2016). To take into account the variations in both model and observed PNSDs,  
400 standard deviations are shown as error bars in the measured and modeled curves based on  
401 BIMN\_Y2020. Three vertical dashed lines at 10 nm, 80 nm, and 250 nm are drawn in (a) to guide  
402 the eye to the four modes discussed in the text.

403  
404

405 The large impacts of nucleation schemes on PNSDs, especially those smaller than 100 nm, can  
406 be seen in Fig. 6. The formation rates and concentrations of nucleation mode particles are very  
407 high based on BHN\_V2002 (peak  $dN_{dlogD_p}$  values reaching well above  $10^3$  std.  $cm^{-3}$ ), negligible  
408 based on BHN\_Y2020 ( $dN_{dlogD_p}$  values for particles  $<10$  nm are generally below 1 std.  $cm^{-3}$ ),  
409 and moderate based on BIMN\_Y2020. When compared to the observed values, the number  
410 concentrations of particles within 3–10 nm based on BHN\_V2002 are 1–2 orders of magnitude  
411 too high but those based on BHN\_Y2020 are 1–2 orders of magnitudes too low, while those based  
412 on BIMN\_Y2020 are of the same order of magnitude. The impact of nucleation schemes on NuclM  
413 propagates into the AitkenM and AccuM1, with BHN\_Y2020 giving the lowest number  
414 concentrations while BHN\_V2002 gives the highest AitkenM and BIMN\_Y2020 gives the highest  
415 AccuM1. It should be noted that, while the line of BHN-Y2020 is lower than that of BIMN and  
416 BHN-V2002 for particles of smaller sizes ( $<\sim 300$  nm), it is slightly higher for larger particles ( $>\sim$   
417 300 nm). This is consistent with the competition of sulfuric acid gas between pre-existing larger  
418 particles and nucleated smaller particles. It is interesting to note that AccuM1 based on  
419 BIMN\_Y2020 is higher than that based on BHN\_V2002 although BHN\_V2002 predicts higher  
420 NuclM and AitkenM, indicating a non-linear interaction among nucleation, growth, and  
421 coagulation. The competition between nucleation and condensation for available sulfuric acid gas  
422 has been shown to be important for SAI studies (Laakso et al., 2022).

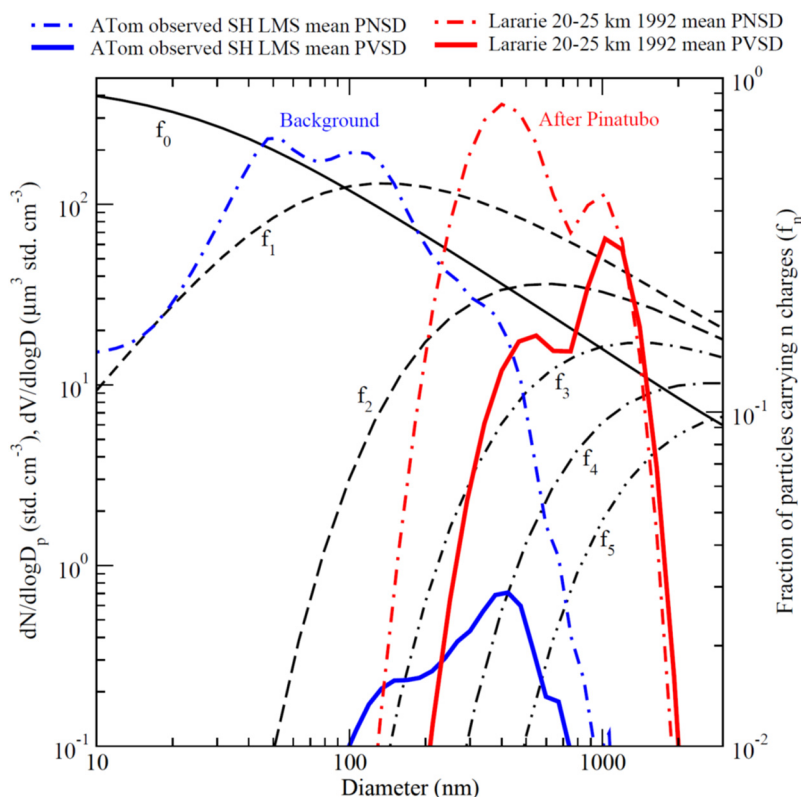
423 There exist a number of differences in the simulated and observed PNSDs. Firstly,  
424 measurements indicate a slight increase of  $dN_{dlogD_p}$  with decreasing sizes for particles  $< 10$  nm  
425 but the simulated PNSDs based on BIMN\_Y2020, the scheme mostly consistent with CLOUD  
426 measurements and predicting NuclM concentrations closest to those observed, decreases with  
427 decreasing sizes for particles  $< 10$  nm. The possible reasons of the difference remain to be  
428 investigated but probably are associated with uncertainty in nucleation rates and size-dependent  
429 growth rates of freshly nucleated particles, and/or the fact that ATom observations are bias towards  
430 daytime. In addition, the small number of particles in this mode is likely within the uncertainty in  
431 the ATom measurements (about 7% of the total number of particles), so that this measured mode  
432 may not be significant. Secondly, the model appears to overpredict the smaller size part ( $\sim 10$ – $40$   
433 nm) of AitkenM although it is close to the larger part of the mode ( $\sim 40$ – $80$  nm). The overprediction  
434 may be a result of the underestimated growth rates or coagulation scavenging rates of these  
435 particles or overpredicted growth rates of NuclM particles. Thirdly, the model generally  
436 overpredicts the mean mode sizes of AccuM1 and underpredicts the concentrations of the mode  
437 except in SH Spring. The nucleation schemes have observable effects on the concentrations and  
438 mean sizes of AccuM1 and overall the simulations based on BIMN\_Y2020 are in stronger  
439 agreement with measurements. Finally, the observed PNSDs show a clear AccuM2 in all seasons  
440 except Fall but such a mode cannot be clearly seen in the model simulated PNSDs, indicating that  
441 the model underpredicts the concentrations of AccuM2 mode particles. AccuM2 particles are

442 within the size range with most efficient scattering of solar radiation and thus are important for  
443 SAI. It is therefore necessary to identify the sources of this difference and to improve the model.

444 As pointed out earlier, the comparison in Fig. 6 does not exactly match in terms of time and  
445 location, which likely contributes to some of the differences shown in Fig. 6. Some of the  
446 differences can also be caused by the uncertainties in the model in term of emissions, transport,  
447 chemistry, aerosol microphysics, and deposition. Nevertheless, some of these differences,  
448 especially the shape of PNSDs (AccuM2, NuclM, etc.), are unlikely to be fully accounted for by  
449 the above-mentioned possible mismatch or model uncertainties and thus may indicate that some  
450 fundamental processes are not represented in the model. One possible cause of the differences is  
451 that the transport of organic-sulfate particles from UT (Murphy et al., 2014, 2021) is not properly  
452 simulated by the model. Based on size-resolved particle composition measurements, Murphy et al.  
453 (2021) showed that the LMS accumulation mode particles (diameter  $\sim 0.1$  and  $1.0 \mu\text{m}$ ) have at  
454 least two modes: the larger mode consists mostly of sulfuric acid particles produced in the  
455 stratosphere, and the smaller mode consists mostly of organic-sulfate particles transported from  
456 the troposphere. Murphy et al. (2014) showed that the fraction of organic-sulfate aerosols above  
457 tropopause decreases quickly with altitudes. While the organic-sulfate mode aerosols from UT  
458 may contribute to the bi-modal structure of accumulation mode particles in the LMS observed  
459 during ATom, it is unlikely to contribute to the bi-modal structure of particles larger than  $\sim 200$  nm  
460 observed at altitude above  $\sim 20$  km both in the background and in volcano perturbed stratosphere  
461 (Deshler et al., 2013, 2019; also see Fig. 7). Here, we suggest that the role of charges on  
462 coagulation and growth of particles in the stratosphere could be another process causing the bi-  
463 modal of large particles in the stratosphere.

464 As shown Fig. 2e, ionization rates are high in LS, ranging from  $\sim 40$ – $100$  ion-pair std.  $\text{cm}^{-3}\text{s}^{-1}$ .  
465 Due to their low number concentrations ( $\sim 100$ – $1000$  std.  $\text{cm}^{-3}$ ) but long lifetime, particles in the  
466 stratosphere are expected to be in charge equilibrium. Figure 7 shows mean particle number size  
467 distribution (PNSD) and particle volume size distribution (PVSD) observed during ATom 1-4 in  
468 SH LMS and measured within 20-25 km altitude over Lararie WY in 1992, and fraction of particles  
469 carrying  $n$  charges based on the modified Boltzmann equilibrium equation (Clement and Harrison,  
470 1992). The bi-modal structure of accumulation mode particles can be clearly seen in both  
471 background and volcano perturbed stratosphere. It should be noted that while the smaller mode  
472 generally dominates the number concentrations, the larger mode dominates mass concentrations.  
473 Under equilibrium more particles are charged (i.e.,  $1-f_0 > 50\%$ ) than neutral ( $f_0$ ) for particles with  
474 diameter larger than  $\sim 80$  nm and a significant fraction ( $> 25\%$ ) of particles larger than 300 nm  
475 carrying multiple charges. While the equilibrium charge fraction is small for NuclM particles ( $\lesssim$   
476 10 nm), this fraction can be much larger when nucleation on ions occurs, which is consistent with  
477 the observed overcharging of freshly nucleated particles (Laakso et al. 2007; Yu and Turco, 2008).  
478 Particle coagulation rates are influenced by forces exerted between colliding particles, including  
479 van der Waals and electrostatic forces, which can modify the effective collision cross section and  
480 sticking coefficient. The van der Waals force has been shown to be important in the stratosphere  
481 (English et al., 2011, 2012) and has been considered in the simulations shown above. The effects  
482 of charges on coagulation and implications for PNSDs in the stratosphere have not yet been studied  
483 (to our knowledge). Since coagulation is a dominant process for the growth of accumulation mode  
484 particles in the stratosphere, we hypothesize that differential coagulation rates for neutral and

485 charged particles in accumulation modes can potentially act as a physical process separating the  
 486 modeled single accumulation mode (Fig. 6) into two modes (AccuM1 and AccuM2) as observed.  
 487 Further research is needed to test this hypothesis. In addition to affecting coagulation, charge on  
 488 small particles can also enhance the growth rate due to ion-dipole interactions of condensing  
 489 molecules with charged particles (Nadykto and Yu, 2005). This enhancement is expected to be  
 490 stronger in the stratosphere because of lower temperature (Nadykto and Yu, 2005). Beside these,  
 491 Svensmark et al. (2020) showed that the condensation of ion clusters can enhance particle growth  
 492 rates. How much the enhanced coagulation and growth rates of charged particles may shape  
 493 PNSDs and modes in the stratosphere remains to be investigated.  
 494



495  
 496 **Figure 7.** ATom 1-4 mean observed particle number size distribution (PNSD, or  $dN/d\log D_p$ ) and  
 497 particle volume size distribution (PVSD, or  $dV/d\log D_p$ ) in SH LMS, balloon-borne measured  
 498 mean PNSD and PVSD within 20-25 km altitude over Lararie WY in 1992, and fraction of  
 499 particles carrying  $n$  ( $n = 0, 1, 2, 3, 4,$  and  $5$ ) charges based on the modified Boltzmann equilibrium  
 500 equation (Clement and Harrison, 1992). Note that  $f_n$  with  $n \geq 1$  including both positive and negative  
 501 charges, i.e., for example, half of  $f_1$  carrying one negative charge while the other half positive.  
 502

#### 503 4. Summary and Discussions

504 Interest in stratospheric aerosols has been increasing in recent years, due to the ongoing  
 505 discussion about the plausibility, potential benefits and risks of offsetting climate change through  
 506 stratospheric aerosol injection (SAI) to buy time for reduction of  $CO_2$  in the atmosphere. Recent  
 507 studies indicate the dependence of SAI radiative efficacy (Dai et al., 2018) on the particle size  
 508 distribution (NASEM, 2021) and thus it is critical to improve foundational understanding and



509 model representation of aerosol microphysics processes controlling the evolution of stratospheric  
510 aerosols, both under background conditions and perturbed scenarios. While formation and growth  
511 of particles in the troposphere have been extensively studied in the past two decades, very limited  
512 efforts have been devoted to understanding these in the stratosphere.

513 In the present study we use both CLOUD laboratory measurements taken under very low  
514 stratospheric temperatures and ATom in-situ observations of particle number size distributions  
515 (PNSD) down to 3 nm to constrain nucleation schemes and model-simulated particle size  
516 distributions in the lowermost stratosphere (LMS). We show that the binary homogenous  
517 nucleation scheme used in most of the existing SAI modeling studies overpredicts the nucleation  
518 rates by 3–4 orders of magnitude (when compared to CLOUD data), leading to significant  
519 overprediction of particle number concentrations in the background stratosphere (by a factor of 2–  
520 4 in SH LMS, compared to ATom data). Based on a recently developed kinetic nucleation model  
521 which provides rates of both ion-mediated nucleation (IMN) and BHN at low temperatures in good  
522 agreement with CLOUD measurements, both BHN and IMN occur in the stratosphere but IMN  
523 rates are generally more than one order of magnitude higher than BHN rates and thus dominate  
524 nucleation in the background stratosphere.

525 In the SH LMS that has minimal influences from anthropogenic emissions, our analysis shows  
526 that ATom-measured PNSDs generally have four apparent modes: a nucleation mode (NuclM:  $\lesssim$   
527 10 nm), which may not be statistically significant, an Aitken mode (AitkenM:  $\sim$ 10–80 nm), and  
528 two accumulation modes (AccuM1:  $\sim$  80–250 nm and AccuM2:  $\sim$  250–700 nm). The model  
529 generally captures the AitkenM and AccuM1 and the existence of a minimum in PNSDs at  $\sim$  80  
530 nm, although there are differences. The model captures a relatively higher AitkenM in SH Summer  
531 and Fall and a higher AccuM1 in SH Spring. The model simulated PNSDs also agree well with  
532 the measurements in term of the size-dependent standard deviations: relatively smaller standard  
533 deviations for AccuM1 and larger size part of AitkenM and much larger standard deviations for  
534 NuclM, smaller size part of AitkenM, and AccuM2.

535 A detailed comparison indicates the existence of a third PNSD mode peaking around 300–400  
536 nm in the ATom measurements that are not captured by the model. Compared to the observations,  
537 the model-simulated AccuM2 standard deviations are larger in SH Winter and Spring but are  
538 smaller in SH Summer and Fall. In addition, the model overpredicts the number concentration of  
539 particles in the size range of 10–50 nm. These differences may indicate that, in addition to  
540 nucleation, the model may be missing some fundamental microphysical processes of stratospheric  
541 aerosols. Our analysis shows that, in the stratosphere, more particles are charged (positive +  
542 negative) than neutral for particles with diameter larger than  $\sim$ 80 nm and a significant fraction ( $>$   
543 25%) of particles larger than 300 nm carrying multiple charges. We propose that the role of charges  
544 on coagulation and growth of particles in the stratosphere, where ionization rates are high and  
545 particles have very long lifetime, is likely one of such processes. Considering the importance of  
546 accurate particle size distributions (especially the accumulation mode particles) for projecting  
547 realistic radiative forcing response to stratospheric aerosols, it is essential to understand and  
548 incorporate such potentially important processes in model simulations of future changes in the  
549 stratosphere. It should be noted that the ATom measurement period does not have a high  
550 stratospheric aerosol loading (i.e., no major volcano eruptions). It remains to be investigated if  
551 previous assessments of volcanic aerosol microphysics missed something important. We expect

552 the uncertainties in the nucleation schemes and unknown cause of the bi-modal structure of  
553 accumulation mode particles will affect particle optical properties and surface area and thus  
554 radiative forcing or chemistry. In addition to what we have shown in this study, there are likely  
555 other uncertainties or missing processes we do not know and the community needs to identify and  
556 resolve these. The present work highlights the importance of advancing scientific understanding  
557 of processes controlling properties of stratospheric particles, identifying important processes -as  
558 well-that the present models might have missed, and as-further development, improvement, and  
559 validation of models for reducing uncertainties of SAI simulations (e.g., Golja et al., 2021, Sun et  
560 al., 2022).

561

562 **Conflict of interest:** The authors declare that they have no conflict of interest.

563

564 **Acknowledgments.** The MERRA-2 data used in this study have been provided by the Global  
565 Modeling and Assimilation Office (GMAO) at NASA Goddard Space Flight Center. This research  
566 has been supported by NASA (grant nos. 80NSSC19K1275 and 80NSSC21K1199) and  
567 SilverLining.

568 **Data availability.** The GEOS-Chem model is available to the public at [https://geos-](https://geos-chem.seas.harvard.edu/)  
569 [chem.seas.harvard.edu/](https://geos-chem.seas.harvard.edu/). Simulation output in this analysis is available at  
570 <https://doi.org/10.5281/zenodo.6909944>. The ATom dataset is published as Wofsy et al., (2021,  
571 <https://doi.org/10.3334/ORNLDAAAC/1925>) and is also available at  
572 <https://espoarchive.nasa.gov/archive/browse/atom> (last access: June 2022).

## 573 **References**

574 Brock, C. A., Hamill, P., Wilson, J. C., Jonsson, H. H., and Chan, K. R.: Particle formation in the  
575 upper tropical troposphere – A source of nuclei for the stratospheric aerosol, *Science*, 270,  
576 1650–1653, <https://doi.org/10.1126/science.270.5242.1650>, 1995.

577 Brock, C. A., Schröder, F., Kärcher, B., Petzold, A., Busen, R., and Fiebig, M.: Ultrafine particle  
578 size distributions measured in aircraft exhaust plumes, *J. Geophys. Res.-Atmos.*, 105, 26555–  
579 26567, <https://doi.org/10.1029/2000jd900360>, 2000.

580 Brock, C. A., Williamson, C., Kupc, A., Froyd, K. D., Erdesz, F., Wagner, N., Richardson, M.,  
581 Schwarz, J. P., Gao, R.-S., Katich, J. M., Campuzano-Jost, P., Nault, B. A., Schroder, J. C.,  
582 Jimenez, J. L., Weinzierl, B., Dollner, M., Bui, T., and Murphy, D. M.: Aerosol size  
583 distributions during the Atmospheric Tomography Mission (ATom): methods, uncertainties,  
584 and data products, *Atmos. Meas. Tech.*, 12, 3081–3099, [https://doi.org/10.5194/amt-12-](https://doi.org/10.5194/amt-12-3081-2019)  
585 3081-2019, 2019.

586 Brock, C.A., Froyd, K.D., Dollner, M., Williamson, C.J., Schill, G., Murphy, D.M., Wagner, N.J.,  
587 Kupc, A., Jimenez, J.L., Campuzano-Jost, P., Nault, B.A., Schroder, J.C., Day, D.A., Price,  
588 D.J., Weinzierl, B., Schwarz, J.P., Katich, J.M., Wang, S., Zeng, L., Weber, R., Dibb, J.,  
589 Scheuer, E., Diskin, G.S., DiGangi, J.P., Bui, T., Dean-Day, J.M., Thompson, C.R., Peischl,  
590 J., Ryerson, T.B., Bourgeois, I., Daube, B.C., Commane, R., and Wofsy, S.C. Ambient  
591 aerosol properties in the remote atmosphere from global-scale in situ measurements, *Atmos.*  
592 *Chem. Phys.*, 21: 15023-63. 2021.

593 Carn, S. A., Yang, K., Prata, A. J. and Krotkov, N. A.: Extending the long-term record of volcanic  
594 SO<sub>2</sub> emissions with the Ozone Mapping and Profiler Suite nadir mapper. *Geophys. Res. Lett.*,  
595 42: 925– 932. doi: 10.1002/2014GL062437, 2015.

596 Clement, C. F., & Harrison, R. G.: The charging of radioactive aerosols. *Journal of Aerosol*  
597 *Science*, 23(5), 481–504. [https://doi.org/10.1016/0021-8502\(92\)90019-R](https://doi.org/10.1016/0021-8502(92)90019-R), 1992.

598 Dai, Z., Weisenstein, D. K., & Keith, D. W.: Tailoring meridional and seasonal radiative forcing  
599 by sulfate aerosol solar geoengineering. *Geophysical Research Letters*, 45, 1030–1039.  
600 <https://doi.org/10.1002/2017GL076472>, 2018.

601 Dawson, M. L., Varner, M. E., Perraud, V., Ezell, M. J., Gerber, R. B., & Finlayson-Pitts, B. J.:  
602 Simplified mechanism for new particle formation from methanesulfonic acid, amines, and  
603 water via experiments and ab initio calculations. *Proceedings of the National Academy of*  
604 *Sciences*, 109(46), 18719-18724, 2012.

605 Dunne, E. M., Gordon, H., Kürten, A., Almeida, J., Duplissy, J., Williamson, C., Ortega, I. K.,  
606 Pringle, K. J., Adamov, A., Baltensperger, U., Barmet, P., Benduhn, F., Bianchi, F.,  
607 Breitenlechner, M., Clarke, A., Curtius, J., Dommen, J., Donahue, N. M., Ehrhart, S., Flagan,  
608 R. C., Franchin, A., Guida, R., Hakala, J., Hansel, A., Heinritzi, M., Jokinen, T., Kangasluoma,  
609 J., Kirkby, J., Kulmala, M., Kupc, A., Lawler, M. J., Lehtipalo, K., Makhmutov, V., Mann,  
610 G., Mathot, S., Merikanto, J., Miettinen, P., Nenes, A., Onnela, A., Rap, A., Reddington, C.  
611 L. S., Riccobono, F., Richards, N. A. D., Rissanen, M. P., Rondo, L., Sarnela, N.,  
612 Schobesberger, S., Sengupta, K., Simon, M., Sipilä, M., Smith, J. N., Stozhkov, Y., Tomé,  
613 A., Tröstl, J., Wagner, P. E., Wimmer, D., Winkler, P. M., Worsnop, D. R., and Carslaw, K.  
614 S.: Global particle formation from CERN CLOUD measurements, *Science*, 354, 1119–1124,  
615 <https://doi.org/10.1126/science.aaf2649>, 2016.

616 Eastham, S. D., Weisenstein, D. K., & Barrett, S. R.: Development and evaluation of the unified  
617 tropospheric–stratospheric chemistry extension (UCX) for the global chemistry-transport  
618 model GEOS-Chem. *Atmospheric Environment*, 89, 52-63, 2014.

619 English, J. M., Toon, O. B., Mills, M. J., & Yu, F.: Microphysical simulations of new particle  
620 formation in the upper troposphere and lower stratosphere. *Atmospheric Chemistry and*  
621 *Physics*, 11(17), 9303-9322, 2011.

622 Evans, M. J., & Jacob, D. J.: Impact of new laboratory studies of N<sub>2</sub>O<sub>5</sub> hydrolysis on global model  
623 budgets of tropospheric nitrogen oxides, ozone, and OH. *Geophysical Research Letters*, 32(9),  
624 2005.

625 Golja, C. M., Chew, L. W., Dykema, J. A., & Keith, D. W.: Aerosol dynamics in the near field of  
626 the SCoPEX stratospheric balloon experiment. *Journal of Geophysical Research:*  
627 *Atmospheres*, 126, e2020JD033438. <https://doi.org/10.1029/2020JD033438>, 2021.

628 Gronoff, G., Berkoff, T., Knowland, K. E., Lei, L., Shook, M., Fabbri, B., Carrion, W., & Langford,  
629 A. O.: Case study of stratospheric intrusion above Hampton, Virginia: lidar-observation and  
630 modeling analysis. *Atmospheric Environment*, 118498, 2021.

631 Hamill, P., Turco, R. P., Kiang, C. S., Toon, O. B., and Whitten, R. C.: An analysis of various  
632 nucleation mechanisms for sulfate particles in the stratosphere, *J. Aerosol Sci.*, 13, 561–585,  
633 1982.

634 Hoesly, R. M., Smith, S. J., Feng, L., Klimont, Z., Janssens-Maenhout, G., Pitkanen, T., Seibert,  
635 J. J., Vu, L., Andres, R. J., Bolt, R. M., Bond, T. C., Dawidowski, L., Kholod, N., Kurokawa,

636 J.-I., Li, M., Liu, L., Lu, Z., Moura, M. C. P., O'Rourke, P. R., and Zhang, Q.: Historical  
637 (1750-2014) anthropogenic emissions of reactive gases and aerosols from the Community  
638 Emissions Data System (CEDS), *Geosci. Model Dev.*, 11, 369-408, 2018.

639 Holmes, C. D., Bertram, T. H., Confer, K. L., Graham, K. A., Ronan, A. C., Wirks, C. K., & Shah,  
640 V.: The role of clouds in the tropospheric NO<sub>x</sub> cycle: A new modeling approach for cloud  
641 chemistry and its global implications. *Geophysical Research Letters*, 46(9), 4980-4990, 2019.

642 IPCC. Climate Change 2021: The Physical Science Basis. Contribution of Working Group I to the  
643 Sixth Assessment Report of the Intergovernmental Panel on Climate Change [Masson-  
644 Delmotte, V., P. Zhai, A. Pirani, S. L. Connors, C. Péan, S. Berger, N. Caud, Y. Chen, L.  
645 Goldfarb, M. I. Gomis, M. Huang, K. Leitzell, E. Lonnoy, J. B. R. Matthews, T. K. Maycock,  
646 T. Waterfield, O. Yelekçi, R. Yu and B. Zhou (eds.)]. Cambridge University Press, 2021.

647 Jones, A., Haywood, J. M., Jones, A. C., Tilmes, S., Kravitz, B., and Robock, A.: North Atlantic  
648 Oscillation response in GeoMIP experiments G6solar and G6sulfur: why detailed modelling  
649 is needed for understanding regional implications of solar radiation management, *Atmos.*  
650 *Chem. Phys.*, 21, 1287–1304, <https://doi.org/10.5194/acp-21-1287-2021>, 2021.

651 Kärcher, B., Turco, R. P., Yu, F., Danilin, M. Y., Weisenstein, D. K., Miake-Lye, R. C., & Busen,  
652 R.: A unified model for ultrafine aircraft particle emissions. *Journal of Geophysical Research:*  
653 *Atmospheres*, 105(D24), 29379-29386, 2000.

654 Keller, C. A., Long, M. S., Yantosca, R. M., Da Silva, A. M., Pawson, S., and Jacob D. J.: HEMCO  
655 v1.0: a versatile, ESMF-compliant component for calculating emissions in atmospheric  
656 models, *Geosci. Model Dev.*, 7, 1409–1417, 2014.

657 Kerminen, V. M., Chen, X., Vakkari, V., Petäjä, T., Kulmala, M., & Bianchi, F.: Atmospheric new  
658 particle formation and growth: review of field observations. *Environmental Research Letters*,  
659 13(10), 103003, 2018.

660 Kirkby, J., Curtius, J., Almeida, J., Dunne, E., Duplissy, J., Ehrhart, S., Franchin, A., Gagné, S.,  
661 Ickes, L., Kürten, A., Kupc, A., Metzger, A., Riccobono, F., Rondo, L., Schobesberger, S.,  
662 Tsagkogeorgas, G., Wimmer, D., Amorim, A., Bianchi, F., Breitenlechner, M., David, A.,  
663 Dommen, J., Downard, A., Ehn, M., Flagan, R. C., Haider, S., Hansel, A., Hauser, D., Jud, W.,  
664 Junninen, H., Kreissl, F., Kvashin, A., Laaksonen, A., Lehtipalo, K., Lima, J., Lovejoy, E. R.,  
665 Makhmutov, V., Mathot, S., Mikkilä, J., Minginette, P., Mogo, S., Nieminen, T., Onnela, A.,  
666 Pereira, P., Petäjä, T., Schnitzhofer, R., Seinfeld, J. H., Sipilä, M., Stozhkov, Y., Stratmann,  
667 F., Tomé, A., Vanhanen, J., Viisanen, Y., Vrtala, A., Wagner, P. E., Walther, H., Weingartner,  
668 E., Wex, H., Winkler, P. M., Carslaw, K. S., Worsnop, D. R., Baltensperger, U., and Kulmala,  
669 M.: The role of sulfuric acid, ammonia and galactic cosmic rays in atmospheric aerosol  
670 nucleation, *Nature*, 476, 429–433, 2011.

671 Kirner, O., Ruhnke, R., Buchholz-Dietsch, J., Jöckel, P., Brühl, C., & Steil, B.: Simulation of polar  
672 stratospheric clouds in the chemistry-climate-model EMAC via the submodel  
673 PSC. *Geoscientific Model Development*, 4(1), 169-182, 2011.

674 Knowland, K. E., Keller, C. A., Wales, P. A., Wargan, K., Coy, L., Johnson, M. S., et al. (2022).  
675 NASA GEOS Composition Forecast Modeling System GEOS-CF v1.0: Stratospheric  
676 composition. *Journal of Advances in Modeling Earth Systems*, 14, e2021MS002852.  
677 <https://doi.org/10.1029/2021MS002852>.

678 Kravitz, B., Robock, A., Boucher, O., Schmidt, H., Taylor, K. E., Stenchikov, G., & Schulz, M.:  
679 The geoengineering model intercomparison project (GeoMIP). *Atmospheric Science*  
680 *Letters*, 12(2), 162-167, 2011.

681 Kulmala, M., Vehkamäki, H., Petäjä, T., Dal Maso, M., Lauri, A., Kerminen, V. M., W. Birmili,  
682 & McMurry, P. H.: Formation and growth rates of ultrafine atmospheric particles: a review  
683 of observations. *Journal of Aerosol Science*, 35(2), 143-176. doi:  
684 10.1016/j.jaerosci.2003.10.003, 2004.

685 Kupc, A., Williamson, C., Wagner, N. L., Richardson, M., & Brock, C. A.: Modification,  
686 calibration, and performance of the Ultra-High Sensitivity Aerosol Spectrometer for particle  
687 size distribution and volatility measurements during the Atmospheric Tomography Mission  
688 (ATom) airborne campaign. *Atmospheric Measurement Techniques*, 11(1), 369-383.  
689 doi:10.5194/amt-11-369-2018, 2018.

690 Kupc, A., Williamson, C. J., Hodshire, A. L., Kazil, J., Ray, E., Bui, T. P., Dollner, M., Froyd, K.  
691 D., McKain, K., Rollins, A., Schill, G. P., Thames, A., Weinzierl, B. B., Pierce, J. R., and  
692 Brock, C. A.: The potential role of organics in new particle formation and initial growth in  
693 the remote tropical upper troposphere, *Atmos. Chem. Phys.*, 20, 15037-15060, 10.5194/acp-  
694 20-15037-2020, 2020.

695 Kürten, A., Bianchi, F., Almeida, J., Kupiainen-Määttä, O., Dunne, E. M., Duplissy, J., Williamson,  
696 C., Barmet, P., Breitenlechner, M., Dommen, J., Donahue, N. M., Flagan, R. C., Franchin,  
697 A., Gordon, H., Hakala, J., Hansel, A., Heinritzi, M., Ickes, L., Jokinen, T., Kangasluoma, J.,  
698 Kim, J., Kirkby, J., Kupc, A., Lehtipalo, K., Leiminger, M., Makhmutov, V., Onnela, A.,  
699 Ortega, I. K., Petäjä, T., Praplan, A. P., Riccobono, F., Rissanen, M. P., Rondo, L.,  
700 Schnitzhofer, R., Schobesberger, S., Smith, J. N., Steiner, G., Stozhkov, Y., Tomé, A., Tröstl,  
701 J., Tsagkogeorgas, G., Wagner, P. E., Wimmer, D., Ye, P., Baltensperger, U., Carslaw, K.,  
702 Kulmala, M., and Curtius, J.: Experimental particle formation rates spanning tropospheric  
703 sulfuric acid and ammonia abundances, ion production rates, and temperatures, *J. Geophys.*  
704 *Res.-Atmos.*, 121, 12377–12400, <https://doi.org/10.1002/2015JD023908>, 2016.

705 Laakso, A., Niemeier, U., Vioni, D., Tilmes, S., and Kokkola, H.: Dependency of the impacts of  
706 geoengineering on the stratospheric sulfur injection strategy – Part 1: Intercomparison of  
707 modal and sectional aerosol modules, *Atmos. Chem. Phys.*, 22, 93–118,  
708 <https://doi.org/10.5194/acp-22-93-2022>, 2022.

709 Laakso, L., Gagné, S., Petäjä, T., Hirsikko, A., Aalto, P. P., Kulmala, M., & Kerminen, V. M.:  
710 Detecting charging state of ultra-fine particles: instrumental development and ambient  
711 measurements. *Atmospheric Chemistry and Physics*, 7(5), 1333-1345, 2007.

712 Lee, S. H., Gordon, H., Yu, H., Lehtipalo, K., Haley, R., Li, Y., & Zhang, R.: New particle  
713 formation in the atmosphere: From molecular clusters to global climate. *Journal of*  
714 *Geophysical Research: Atmospheres*, 124(13), 7098-7146, 2019.

715 Lee, S. H., Reeves, J. M., Wilson, J. C., Hunton, D. E., Viggiano, A. A., Miller, T. M., Ballenthin,  
716 J. O., and Lait, L. R.: Particle formation by ion nucleation in the upper troposphere and lower  
717 stratosphere, *Science*, 301, 1886–1889, <https://doi.org/10.1126/science.1087236>, 2003.

718 Li, M., Zhang, Q., Kurokawa, J.-I., Woo, J.-H., He, K., Lu, Z., Ohara, T., Song, Y., Streets, D. G.,  
719 Carmichael, G. R., Cheng, Y., Hong, C., Huo, H., Jiang, X., Kang, S., Liu, F., Su, H., and  
720 Zheng, B.: MIX: a mosaic Asian anthropogenic emission inventory under the international

721 collaboration framework of the MICS-Asia and HTAP, *Atmos. Chem. Phys.*, 17, 935–963,  
722 <https://doi.org/10.5194/acp-17-935-2017>, 2017.

723 Lockley, A., MacMartin, D., & Hunt, H.: An update on engineering issues concerning stratospheric  
724 aerosol injection for geoengineering. *Environmental Research Communications*, 2(8),  
725 082001, 2020.

726 Lovejoy, E. R., Curtius, J., and Froyd, K. D.: Atmospheric ion-induced nucleation of sulfuric acid  
727 and water, *J. Geophys. Res.*, 109, D08204, <https://doi.org/10.1029/2003JD004460>, 2004.

728 Luo, G., Yu, F., & Moch, J. M.: Further improvement of wet process treatments in GEOS-Chem  
729 v12. 6.0: impact on global distributions of aerosols and aerosol precursors. *Geoscientific*  
730 *Model Development*, 13(6), 2879-2903, 2020.

731 Martin, R. V., Jacob, D. J., Chance, K., Kurosu, T. P., Palmer, P. I., & Evans, M. J.: Global  
732 inventory of nitrogen oxide emissions constrained by space-based observations of NO<sub>2</sub>  
733 columns. *Journal of Geophysical Research: Atmospheres*, 108(D17), 2003.

734 Mills, M. J., Richter, J. H., Tilmes, S., Kravitz, B., MacMartin, D. G., Glanville, A. A., Tribbia, J.  
735 J., Lamarque, J.-F., Vitt, F., Schmidt, A., and Gettelman, A.: Radiative and chemical response  
736 to interactive stratospheric sulfate aerosols in fully coupled CESM1 (WACCM), *J. Geophys.*  
737 *Res.*, 122, 13061–13078, <https://doi.org/10.1002/2017JD027006>, 2017.

738 Murphy, D. M., Froyd, K. D., Bourgeois, I., Brock, C. A., Kupc, A., Peischl, J., Schill, G. P.,  
739 Thompson, C. R., Williamson, C. J., and Yu, P.: Radiative and chemical implications of the  
740 size and composition of aerosol particles in the existing or modified global stratosphere,  
741 *Atmos. Chem. Phys.*, 21, 8915-8932, [10.5194/acp-21-8915-2021](https://doi.org/10.5194/acp-21-8915-2021), 2021.

742 Murray, L. T., Jacob, D. J., Logan, J. A., Hudman, R. C., & Koshak, W. J.: Optimized regional  
743 and interannual variability of lightning in a global chemical transport model constrained by  
744 LIS/OTD satellite data. *Journal of Geophysical Research: Atmospheres*, 117(D20), 2012.

745 Nadykto, A. B., & Yu, F.: Simple correction to the classical theory of homogeneous nucleation.  
746 *The Journal of chemical physics*, 122(10), 104511, 2005.

747 NASEM: Reflecting Sunlight: Recommendations for Solar Geoengineering Research and  
748 Research Governance. Washington, DC: The National Academies Press, 2021.

749 Pye, H. O., & Seinfeld, J. H.: A global perspective on aerosol from low-volatility organic  
750 compounds. *Atmospheric Chemistry and Physics*, 10(9), 4377-4401, 2010.

751 Richter, J., Vioni, D., MacMartin, D., Bailey, D., Rosenbloom, N., Lee, W., Tye, M., and  
752 Lamarque, J.-F.: Assessing Responses and Impacts of Solar climate intervention on the Earth  
753 system with stratospheric aerosol injection (ARISE-SAI), *EGUsphere* [preprint],  
754 <https://doi.org/10.5194/egusphere-2022-125>, 2022.

755 Rotman, D. A., Tannahill, J. R., Kinnison, D. E., Connell, P. S., Bergmann, D., Proctor, D., ... &  
756 Kawa, S. R.: Global Modeling Initiative assessment model: Model description, integration,  
757 and testing of the transport shell. *Journal of Geophysical Research: Atmospheres*, 106(D2),  
758 1669-1691, 2001.

759 Shepherd, J. G.: *Geoengineering the climate: science, governance and uncertainty*. Royal Society,  
760 2009.

761 Shi, Q., Jayne, J. T., Kolb, C. E., Worsnop, D. R., & Davidovits, P.: Kinetic model for reaction of  
762 ClONO<sub>2</sub> with H<sub>2</sub>O and HCl and HOCl with HCl in sulfuric acid solutions. *Journal of*  
763 *Geophysical Research: Atmospheres*, 106(D20), 24259-24274, 2001.

764 Stettler, M.E.J., S. Eastham, S.R.H. Barrett (2011), Air quality and public health impacts of UK  
765 airports. Part I: Emissions, *Atmos. Environ.*, 45, 5415-5424, 2011.

766 Stier, P., Feichter, J., Kinne, S., Kloster, S., Vignati, E., Wilson, J., Ganzeveld, L., Tegen, I.,  
767 Werner, M., Balkanski, Y., Schulz, M., Boucher, O., Minikin, A., and Petzold, A.: The  
768 aerosol-climate model ECHAM5-HAM, *Atmos. Chem. Phys.*, 5, 1125–1156,  
769 <https://doi.org/10.5194/acp-5-1125-2005>, 2005.

770 Sun, H., Eastham, S., & Keith, D.: Developing a Plume-in-Grid model for plume evolution in the  
771 stratosphere. *Journal of Advances in Modeling Earth Systems*, 14, e2021MS002816.  
772 <https://doi.org/10.1029/2021MS002816>, 2022.

773 Svensmark, J., Shaviv, N. J., Enghoff, M. B., & Svensmark, H.: The ION-CAGE code: A  
774 numerical model for the growth of charged and neutral aerosols. *Earth and Space Science*. 7,  
775 e2020EA001142. <https://doi.org/10.1029/2020EA001142>, 2020.

776 Thompson, C.R., Wofsy, S.C., Prather, M.J., Newman, P.A., Hanisco, T.F., Ryerson, T.B., Fahey,  
777 D.W., Apel, E.C., Brock, C.A., Brune, W.H., Froyd, K., Katich, J.M., Nicely, J.M., Peischl,  
778 J., Ray, E., Veres, P.R., Wang, S., Allen, H.M., Asher, E., Bian, H., Blake, D., Bourgeois, I.,  
779 Budney, J., Bui, T.P., Butler, A., Campuzano-Jost, P., Chang, C., Chin, M., Commane, R.,  
780 Correa, G., Crouse, J.D., Daube, B., Dibb, J.E., DiGangi, J.P., Diskin, G.S., Dollner, M.,  
781 Elkins, J.W., Fiore, A.M., Flynn, C.M., Guo, H., Hall, S.R., Hannun, R.A., Hills, A., Hintsä,  
782 E.J., Hodzic, A., Hornbrook, R.S., Huey, L.G., Jimenez, J.L., Keeling, R.F., Kim, M.J., Kupc,  
783 A., Lacey, F., Lait, L.R., Lamarque, J.-F., Liu, J., McKain, K., Meinardi, S., Miller, D.O.,  
784 Montzka, S.A., Moore, F.L., Morgan, E.J., Murphy, D.M., Murray, L.T., Nault, B.A.,  
785 Neuman, J.A., Nguyen, L., Gonzalez, Y., Rollins, A., Rosenlof, K., Sargent, M., Schill, G.,  
786 Schwarz, J.P., Clair, J.M.S., Steenrod, S.D., Stephens, B.B., Strahan, S.E., Strode, S.A.,  
787 Sweeney, C., Thames, A.B., Ullmann, K., Wagner, N., Weber, R., Weinzierl, B., Wennberg,  
788 P.O., Williamson, C.J., Wolfe, G.M., and Zeng, L. 'The NASA Atmospheric Tomography  
789 (ATom) Mission: Imaging the Chemistry of the Global Atmosphere', *Bulletin of the*  
790 *American Meteorological Society*, 103: E761-E90. 2022.

791 Tilmes, S., Mills, M. J., Niemeier, U., Schmidt, H., Robock, A., Kravitz, B., Lamarque, J.-F., Pitari,  
792 G., and English, J. M.: A new Geoengineering Model Intercomparison Project (GeoMIP)  
793 experiment designed for climate and chemistry models, *Geosci. Model Dev.*, 8, 43–49,  
794 <https://doi.org/10.5194/gmd-8-43-2015>, 2015.

795 Turco, R. P., Whitten, R. C., & Toon, O. B.: Stratospheric aerosols: Observation and theory.  
796 *Reviews of Geophysics*, 20(2), 233-279. doi: 10.1029/RG020i002p00233, 1982.

797 van der Werf, G. R., J. T. Randerson, L. Giglio, T. T. van Leeuwen, Y. Chen, B. M. Rogers, M.  
798 Mu, M. J. E. van Marle, D. C. Morton, G. J. Collatz, R. J. Yokelson, and P. S. Kasibhatla,  
799 Global fire emissions estimates during 1997–2016, *Earth Sys. Sci. Data*, 9, 697-720, 2017.

800 van Donkelaar, A., Martin, R.V., Leaitch, W.R., Macdonald, A.M., Walker, T.W., Streets, D.G.,  
801 Zhang, Q., Dunlea, E.J., Jimenez, J.L., Dibb, J.E., Huey, L.G., Weber, R., Andreae, M.O.:  
802 Analysis of aircraft and satellite measurements from the Intercontinental Chemical Transport  
803 Experiment (INTEX-B) to quantify long-range transport of East Asian sulfur to  
804 Canada. *Atmospheric Chemistry and Physics*, 8(11), 2999-3014, 2008.

805 Vehkamäki, H., Kulmala, M., Napari, I., Lehtinen, K. E., Timmreck, C., Noppel, M., & Laaksonen,  
806 A.: An improved parameterization for sulfuric acid–water nucleation rates for tropospheric

807 and stratospheric conditions. *Journal of Geophysical Research: Atmospheres*, 107(D22),  
808 AAC-3. doi: 10.1029/2002JD002184, 2002.

809 Weisenstein, D. K., Visioni, D., Franke, H., Niemeier, U., Vattioni, S., Chiodo, G., Peter, T., and  
810 Keith, D. W.: An interactive stratospheric aerosol model intercomparison of solar  
811 geoengineering by stratospheric injection of SO<sub>2</sub> or accumulation-mode sulfuric acid  
812 aerosols, *Atmos. Chem. Phys.*, 22, 2955–2973, <https://doi.org/10.5194/acp-22-2955-2022>,  
813 2022.

814 Williamson, C., Kupc, A., Wilson, J., Gesler, D. W., Reeves, J. M., Erdesz, F., McLaughlin, R., &  
815 Brock, C. A.: Fast time response measurements of particle size distributions in the 3-60 nm  
816 size range with the nucleation mode aerosol size spectrometer. *Atmospheric Measurement*  
817 *Techniques*, 11(6), 3491-3509. doi:10.5194/amt-11-3491-2018, 2018.

818 Williamson, C. J., Kupc, A., Axisa, D., Bilsback, K. R., Bui, T., Campuzano-Jost, P., Dollner, M.,  
819 Froyd, K. D., Hodshire, A. L., Jimenez, J. L., Kodros, J. K., Luo, G., Murphy, D. M., Nault,  
820 B. A., Ray, E. A., Weinzierl, B., Wilson, J. C., Yu, F. Q., Yu, P. F., Pierce, J. R., and Brock,  
821 C. A.: A large source of cloud condensation nuclei from new particle formation in the tropics,  
822 *Nature*, 574, 399–403, <https://doi.org/10.1038/s41586-019-1638-9>, 2019.

823 Williamson, C. J., Kupc, A., Rollins, A., Kazil, J., Froyd, K. D., Ray, E. A., Murphy, D. M., Schill,  
824 G. P., Peischl, J., Thompson, C., Bourgeois, I., Ryerson, T. B., Diskin, G. S., DiGangi, J. P.,  
825 Blake, D. R., Bui, T. P. V., Dollner, M., Weinzierl, B., and Brock, C. A.: Large hemispheric  
826 difference in nucleation mode aerosol concentrations in the lowermost stratosphere at mid-  
827 and high latitudes, *Atmos. Chem. Phys.*, 21, 9065–9088, [https://doi.org/10.5194/acp-21-](https://doi.org/10.5194/acp-21-9065-2021)  
828 [9065-2021](https://doi.org/10.5194/acp-21-9065-2021), 2021.

829 Wofsy, S.C., S. Afshar, H.M. Allen, E.C. Apel, E.C. Asher, B. Barletta, J. Bent, H. Bian, B.C.  
830 Biggs, D.R. Blake, N. Blake, I. Bourgeois, C.A. Brock, W.H. Brune, J.W. Budney, T.P. Bui,  
831 A. Butler, P. Campuzano-Jost, C.S. Chang, M. Chin, R. Commane, G. Correa, J.D. Crouse,  
832 P. D. Cullis, B.C. Daube, D.A. Day, J.M. Dean-Day, J.E. Dibb, J.P. DiGangi, G.S. Diskin,  
833 M. Dollner, J.W. Elkins, F. Erdesz, A.M. Fiore, C.M. Flynn, K.D. Froyd, D.W. Gesler, S.R.  
834 Hall, T.F. Hanisco, R.A. Hannun, A.J. Hills, E.J. Hints, A. Hoffman, R.S. Hornbrook, L.G.  
835 Huey, S. Hughes, J.L. Jimenez, B.J. Johnson, J.M. Katich, R.F. Keeling, M.J. Kim, A. Kupc,  
836 L.R. Lait, K. McKain, R.J. McLaughlin, S. Meinardi, D.O. Miller, S.A. Montzka, F.L. Moore,  
837 E.J. Morgan, D.M. Murphy, L.T. Murray, B.A. Nault, J.A. Neuman, P.A. Newman, J.M.  
838 Nicely, X. Pan, W. Paplawsky, J. Peischl, M.J. Prather, D.J. Price, E.A. Ray, J.M. Reeves, M.  
839 Richardson, A.W. Rollins, K.H. Rosenlof, T.B. Ryerson, E. Scheuer, G.P. Schill, J.C.  
840 Schroder, J.P. Schwarz, J.M. St.Clair, S.D. Steenrod, B.B. Stephens, S.A. Strode, C. Sweeney,  
841 D. Tanner, A.P. Teng, A.B. Thames, C.R. Thompson, K. Ullmann, P.R. Veres, N.L. Wagner,  
842 A. Watt, R. Weber, B.B. Weinzierl, P.O. Wennberg, C.J. Williamson, J.C. Wilson, G.M.  
843 Wolfe, C.T. Woods, L.H. Zeng, and N. Vieznor. 2021. ATom: Merged Atmospheric  
844 Chemistry, Trace Gases, and Aerosols, Version 2. ORNL DAAC, Oak Ridge, Tennessee,  
845 USA. <https://doi.org/10.3334/ORNLDAAC/1925>.

846 Yu, F., & Luo, G.: Simulation of particle size distribution with a global aerosol model: contribution  
847 of nucleation to aerosol and CCN number concentrations. *Atmospheric Chemistry and*  
848 *Physics*, 9(20), 7691-7710, 2009.



849 Yu, F., & Turco, R. P.: Ultrafine aerosol formation via ion-mediated nucleation. *Geophysical*  
850 *Research Letters*, 27(6), 883-886. doi: 10.1029/1999GL011151, 2000.

851 Yu, F., Nadykto, A. B., Herb, J., Luo, G., Nazarenko, K. M., & Uvarova, L. A.: H<sub>2</sub>SO<sub>4</sub>-H<sub>2</sub>O-NH<sub>3</sub>  
852 ternary ion-mediated nucleation (TIMN): kinetic-based model and comparison with CLOUD  
853 measurements. *Atmospheric Chemistry and Physics*, 18(23), 17451-17474, 2018.

854 Yu, F., Nadykto, A. B., Luo, G., & Herb, J.: H<sub>2</sub>SO<sub>4</sub>-H<sub>2</sub>O binary and H<sub>2</sub>SO<sub>4</sub>-H<sub>2</sub>O-NH<sub>3</sub> ternary  
855 homogeneous and ion-mediated nucleation: lookup tables version 1.0 for 3-D modeling  
856 application. *Geoscientific Model Development*, 13(6), 2663-2670, 2020.

857 Zhang, R., Khalizov, A., Wang, L., Hu, M., & Xu, W.: Nucleation and growth of nanoparticles in  
858 the atmosphere. *Chemical reviews*, 112(3), 1957-2011, 2012.

859